LUNDS UNIVERSITET

Optimization and Characterization of Luminescent Materials for the ESS Proton Beam Imaging System

Anton Järild & Emelie Wiklund

Master Thesis 2021

DEGREE PROJECT IN MATERIALS CHEMISTRY
LUND, SWEDEN 2021

Supervisors:

Monika Hartl
Sample Handling and User Labortory, ESS ERIC

Cyrille Thomas
Beam Diagnostics, ESS ERIC

Martin Ek Rosén
Centre for Analysis and Synthesis
Faculty of Engineering, Lund University

Examinator:

Reine Wallenberg
Centre for Analysis and Synthesis
Faculty of Engineering, Lund University

Acronyms

BET Brunauer–Emmett–Teller

CL Cathodoluminescence

DSC Differential Scanning Calorimetry

EDS Energy-Dispersive X-ray Spectroscopy

EL Electroluminescence

ESS European Spallation Source

FCC Face-Centred Cubic

HCP Hexagonally Close-Packed

IL Ionoluminescence

IR Infrared

LED Light Emitting Diode

LUMO Lowest Unoccupied Molecular Orbital

PL Photoluminesence

PBI Proton Beam Imaging

PXRD Powder X-Ray Diffraction

SEM Scanning Electron Microscopy

SE Secondary Electrons

SNS Spallation Neutron Source at Oak Ridge National Laboratory

TG Thermogravimetry

UV Ultra-Violet

XRD X-ray Diffraction

XRF X-ray Fluorescence

YAG Yttrium-Aluminum-Garnet

YAP Yttrium-Aluminum-Perovskite

Abstract

Spallation sources such as European Spallation Source (ESS) produces neutrons by bombarding high-energy protons onto the target wheel. To determine the location of the proton beam a Proton Beam Imaging (PBI) system will be installed. The PBI system at ESS relies on the properties of a luminescent coating that is sprayed onto the target wheel and the proton beam window. In this study, luminescent materials for the PBI system are investigated and evaluated on their luminescent properties using photoluminescence spectroscopy. The material in focus is the Cr-doped alumina, which has been investigated in two parts. Sprayed coatings, made from an existing precursor, are investigated to understand how the luminescent behavior of Cr-doped alumina is affected by various factors in the ESS environment. Thereafter, a new Cr-doped alumina precursor is developed and optimized to produce a coating with superior properties.

The existing precursor from the sprayed sample consists of a mixture of Al_2O_3 and Cr_2O_3 that reacts during spraying to form Cr-doped alumina. This study compared the luminescent properties of two spraying techniques: plasma-spray and flame-spray. The results show that plasma spraying produces brighter coatings than flame spraying due to lower presence of the undesired η-alumina phase in the finished coating. The coating thickness optimization showed that 100 µm gave the brightest coating. Pure Cr_2O_3 was found in all of the sprayed samples, which indicates that full incorporation of Cr_2O_3 into alumina has been unsuccessful.

In this study, a new Cr-doped alumina precursor is proposed in which the powder is sintered prior to thermal spraying. Pre-sintering of the precursor material is suggested to produce a more controlled, homogeneous and complete incorporation of the Cr^{3+}-ions into the alumina matrix, hence producing a coating with superior luminescent properties. Pink, bright luminescent Cr-doped alumina powders were successfully prepared via two synthesis routes, the solid-state and solution-based synthesis, and compared based on their luminescent properties after heat treatment at different temperatures. The solution-based samples exhibited superior luminescence at temperatures of 1100 °C and 1300 °C, which is due to earlier transition into the η and α-alumina phase. Sintering powders at 1550 °C gave equally bright materials from both syntheses. The optimal doping concentration of Cr^{3+}-ions was 1 wt% of Cr_2O_3. To spray the precursors, the particle size needs to be in the range of 5-60 µm to give satisfactory results. Therefore, the effect of ball milling on luminescence was studied. It was discovered that high-energy ball milling reduced the luminescence intensity significantly due to the violent crushing of the alumina crystals. Grinding the particles with a mortar and pestle could reduce the particle size sufficiently without the material losing its luminescent properties.

For the last part of this study, two alternative materials for the PBI system were investigated: Ti-doped alumina and Ce-doped YAG. The Ti-doped alumina powder showed no luminescent properties and the study continued with Ce-doped YAG. This material was successfully produced, which created a yellow powder that exhibited a broad emission from the green to yellow region upon blue light excitation. A doping concentration screening that was performed revealed that 1.6 mol% gave the brightest material.

Populärvetenskaplig sammanfattning

Självlysande material ska hjälpa ESS att detektera protoner

Protonstrålning används för att generera neutroner på ESS; en effektiv metod som kommer ge ESS världsledande prestanda, men som medför utmaningar. Den högenergetiska protonstrålen kan inte ses med blotta ögat och kan potentiellt skada instrument, vilket leder till att övervaka protonstrålen blir svårt, men kritiskt. Lösningen är ett självlysande material som skapar en bild av var protonstrålen träffar.

Det sameuropeiska forskningsprojektet European Spallation Source (ESS) byggs för närvarande i Lund och förväntas bli färdigställt år 2023. Forskningsanläggningen kommer då att använda neutroner för att studera material på atomär nivå för att bryta ny mark inom biologi, kemi, fysik, geologi och medicin. För att skapa en neutronpuls på ESS kommer en roterande målskiva gjord av volfram att bli bestrålad av en högenergetisk protonstråle. Protonerna träffar målskivan med 94% av ljusets hastighet, vilket gör att protonerna tränger in i materialet och slår ut neutroner från volframkärnorna. På grund av dess oerhörda energi kan protonstrålen, om den är fel inställd och belyser oönskade områden, skada dyr utrustning som även kan bli en säkerhetsrisk. Därför är det av oerhörd vikt att övervaka och säkerställa protonstrålens status i alla lägen. Eftersom protoner inte är synliga med blotta ögat har ESS planerat att installera ett avbildningssystem av protonstrålen. Principen är att spraya en tunn ytbeläggning av ett självlysande material på målskivan. När protonstrålen penetrerar det självlysande materialet genereras fotoner. Dessa fotoner detekteras av kamerasystem för att skapa en avbildning i realtid av protonstrålen med millimeterprecision. Den påfrestande miljön av det högteknologiska ändamålet sätter höga krav på den luminescerande ytbeläggningen. Därför har ESS påbörjat ett samarbete med ett flertal forskningsinstitut för att utveckla ett lämpligt material innan ESS sätts i drift.

Detta examensarbete har undersökt och optimerat luminescerande material för protonstråleavbildning. Materialen som har behandlats i studien är dopade, kristallina material. Dopning är en process där en liten andel av ett främmande ämne avsiktligt introduceras i en struktur för att ändra materialets egenskaper. En följd av doping kan vara att ett material får självlysande, eller 'luminescerande', egenskaper. Materialet i huvudfokus i denna studie har varit krom-dopat aluminiumoxid, även känt som rubin, vilket är ett material som tidigare har studerats för detta ändamål. Av listan på krav valdes ett antal ut att utvärdera under denna studie, varav ljusstyrka var en av dem.

Först undersöktes färdigsprayade ytbeläggningar av krom-dopat aluminiumoxid. Dessa hade tillverkats av ett pulver inköpt från en materialleverantör i U.S.A. Pulvret bestod av kromoxid och aluminiumoxid som, när det sprayas reagerar och bildar kromdopat aluminiumoxid. Resultat från diverse analysmetoder visade att kromoxiden inte hade lösts upp fullständigt i aluminiumoxiden, vilket antydde på att det inköpta pulvret inte var optimerat och att materialet kunde uppnå bättre egenskaper. ESS önskar att kunna producera ett eget pulver med optimala luminescerande egenskaper vilket motiverade utveckling av ett nytt pulver av krom-dopat aluminiumoxid.

Därför utvärderades två nya syntesmetoder för att producera pulver med luminescerande egenskaper. Genom att värmebehandla pulvret innan sprayning genomförs en fulländad och kontrollerad doping. Resultaten visade att båda syntesmetoderna skapade krom-dopat aluminiumoxidpulver med starkt luminescerande egenskaper. Efter tillräckligt hög värmebehandling omvandlades pulvret från grön till rosa, vilket tydde på dopningen hade genomförts och att rätt kristallstruktur av aluminiumoxiden var uppnådd. Ljusstyrkan hos materialet ökade med temperaturen på värmehandlingen, vilket berodde på ökad dopningsgrad och även omvandling till mer gynnsamma kristallstrukturer. Kristallstorleken visade sig påverka luminiscensen då större kristaller gav starkare luminescerande förmåga och att vissa malningsstekniker därför dämpar luminiscensstyrkan i produkten. Efter optimering kunde det nya pulvret produceras i stor-skala för testsprayning.

Denna studie har bidragit till att ESS är ännu ett steg närmare att ha ett fungerande luminiscernade material innan ESS är i drift och första protonerna når målskivan.

Acknowledgement

This project was performed at the European Spallation Source (ERIC) under the divisions 'Beam diagnostics' and 'Users laboratory' as a master thesis for the master's program in chemical engineering at Lund University. The study falls under the collaboration between European Spallation Source (ERIC), University West, the Spallation Neutron Source and the University of Oslo for the development of luminescent coatings for proton beam imaging. In this work, materials are thoroughly investigated, evaluated and optimized based on their luminescent properties.

A special thanks to our two supervisors at ESS, Monika Hartl and Cyrille Thomas, for making this master thesis possible and for your enthusiasm, support and guidance through the entire project. Thanks to Martin Ek Rosén for tirelessly assisting us, but also giving feedback in the writing process of this thesis. We would also like to thank the 'Sample handling and user labs' team at ESS for your warm and welcoming atmosphere, for adapting, in these pandemic times, to let us use the ESS laboratories and facilities.

Contents

1 Introduction

With the world's most powerful neutron source and a suite of state-of-the-art neutron instruments, European Spallation Source (ESS) will enable great opportunities for scientific discovery in various fields. The development of pharmaceuticals, foods, textiles, computers, fuel cells, superconductors and much more profit from the advancement of neutron scattering science. The quality of the results from neutron experiments strongly depends on the brightness of the neutron source. Collisions of high-energy protons and the tungsten target leads to scattering of neutrons. To monitor the proton beam, an imaging system with two luminescent screens will be installed in the target area [1]. The photons emitted from the screens will be the only source to provide information about the status of the beam at all times, making it a vital part of the complex machinery that is ESS. The facility will have the most powerful linear proton accelerator ever built, which puts high demands on the luminescent material in the harsh environment. To this date, there is no luminescent material discovered that fulfills all the requirements of the Proton Beam Imaging (PBI) system at ESS. The research made on luminescent screens for this high-technological and specific application is limited, which enables possibilities to break new ground in the field of optimization and characterization of these materials. In this study, we explore the properties of several luminescent materials including the influence of crystal structures, synthesis routes, crystallite size and doping on luminescence.

1.1 Overview of ESS

The ESS is one of the largest science and technology infrastructures that is being built today. The facility, located on the outskirts of Lund, Sweden, is currently under construction and is planned to produce neutrons in 2023. The revolutionizing technology of the neutron spallation at the ESS facility will produce 30-100 times brighter neutron beams than the beams produced from nuclear reactors [2].

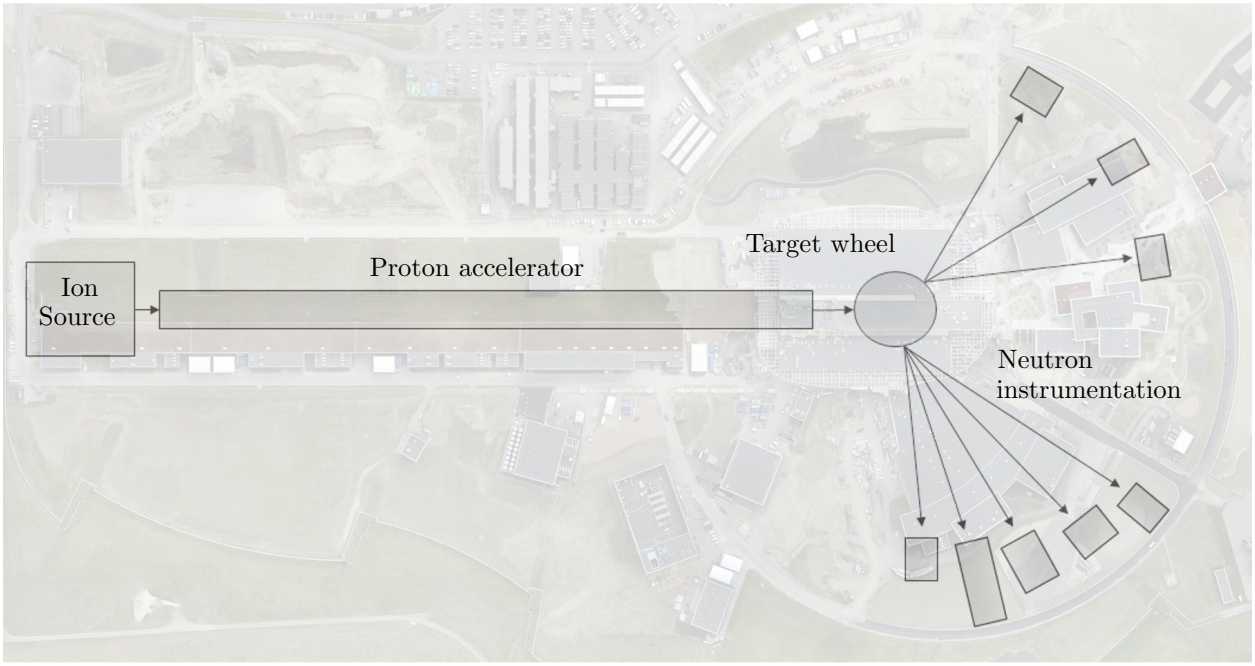

Figure 1: A schematic image of the main components of ESS. Protons are generated in the ion source, then accelerated through the linear proton accelerator. The protons collide with the target wheel in which neutrons scatters and are then lead to the neutron instrumentation. Aerial photo credit: ESS

A schematic overview of the main components of ESS is shown in Figure 1. The first step in the neutron spallation is the proton production in an ion source. Hydrogen gas is heated by subjecting it to rapidly

oscillating electromagnetic fields, which eventually results in electron evaporation of the hydrogen molecules. The remaining proton plasma is then transferred to the ion accelerator, where the protons are accelerated by magnets, electromagnetic fields and superconducting cavities over 600 meters. The protons reach 94 % of the speed of light at the end of the linear accelerator, where they hit the so-called target wheel, a 2.6 m diameter, helium-cooled, rotating disk made of tungsten bricks. The high-energy protons collide with the tungsten atoms, which leads to scattering of high-energy neutrons. The generated neutrons are moderated and then led onward to the instruments for neutron science experiments [3].

1.1.1 Proton beam imaging system

The linear proton accelerator will send 2.8 ms long pulses of 2 GeV protons with a frequency of 14 Hz onto the rotating target wheel and is expected to run 5000 h per year. Due to its high power, it is of great importance to control the proton beam since illuminating undesired areas can cause damage to the target. Therefore, special magnets will raster the beam onto the target, creating a controlled and uniformly distributed illuminated area [1]. An imaging system, which is illustrated in Figure 2, will be installed in the target region in order to monitor the proton beam [1]. The imaging system will consists of two luminescent screens. The first screen will be sprayed onto the proton beam window, a thin, water-cooled aluminum plate that separates the accelerator region and the target region [4]. The second luminescent screen will be sprayed onto the surface of the target wheel housing itself.

The principle behind the beam monitoring is to spray a thin layer (thickness is tenths of mm) of a luminescent material onto the target wheel housing and the proton beam window. As the luminescent coating is bombarded with protons, it will emit electromagnetic radiation that is collected with optical fibers and camera systems. In that way, real-time imaging of the proton beam is obtained, which enables to tune and verify the status of the proton beam at all times [1]. The installation of a reliable PBI system on the target wheel can therefore reassure the safety of the multi-million euro equipment that is the target wheel. This sets high demands on the functionality of the imaging system, not least the luminescent coating.

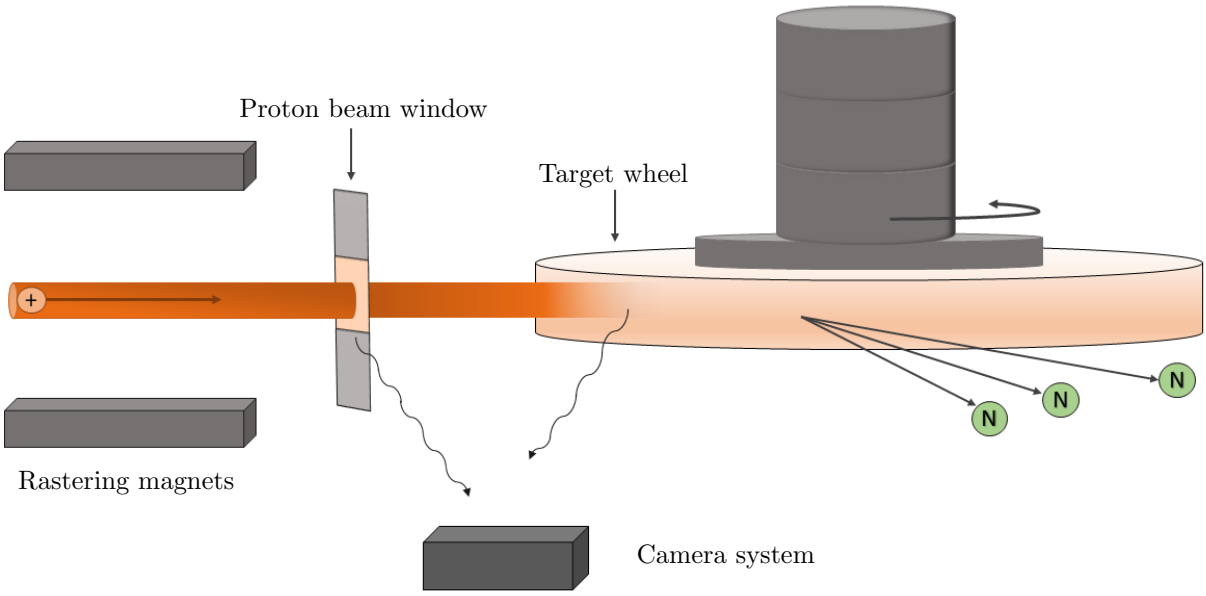

Figure 2: A schematic image of the main components in the PBI system. Two luminescent screens are sprayed onto the proton beam window and the target wheel housing.

1.2 Requirements of the luminescent coating

The ESS design of PBI system using luminescent materials has been tried and evaluated at the Spallation Neutron Source at Oak Ridge National Laboratory (SNS), a similar neutron spallation research facility in the United States. Based on the studies done at SNS and ESS, a long list of requirements for the characteristics of the luminescent material has been unraveled. To avoid the beam damaging the target, it is crucial to find a material that can satisfy the following requirements;

- **Sufficiently high photon yield** - To obtain satisfactory imaging quality, the material is required to emit a large enough signal-to-noise ratio.
- **The emission spectrum** - the emission spectrum of the material should be efficient to collect for the imaging system. In the high radiation environment, other materials or elements can emit light. In order to reduce this noise, the emission spectrum should be distinctive from possible fluorescent materials of the target area.
- **The fluorescence lifetime** is the time a fluorophore, on average, spend in an excited state before emitting a photon and returning to its ground state - in other words, the time for a luminescent material to emit light after it has been activated [5]. A long luminescent lifetime in combination with the rotation of the target wheel creates a streak effect in the image, which can be seen in Figure 3. The left image shows the image obtained from a non-moving target, the proton beam window. The right shows an image of the moving target, the target wheel. When looking at the moving target, the luminescence appears outside of the allocated requirements (the white rectangle). To be able to see the exact position of the probe and form an image that reflects reality without the streak effect, a material with a shorter luminescent lifetime is needed.

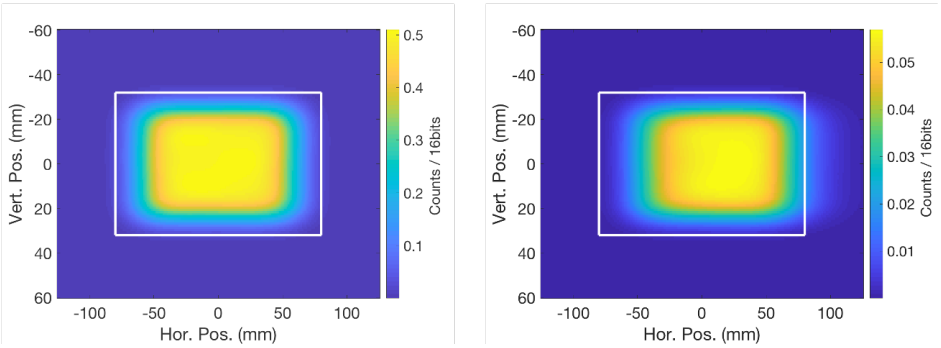

Figure 3: The left figure is a simulation of the proton beam window where the white rectangle indicates the allocated requirements. The right figure shows a simulation of the target wheel with more significant uncertainties in the horizontal axis.

- **Radiation tolerance** - From early studies at SNS it was observed that the chosen luminescent coating exponentially lost its luminescence upon radiation. After 100-200 MWh of radiation, the luminescence had reached a minimum. Spraying the material onto the target wheel will not allow frequent replacement of the luminescent coating. Therefore, the radiation tolerance needs to be sufficient to operate for a longer time.
- **Corrosion resistance** - The target wheel will operate in a low vacuum environment, resulting in a small presence of N_2, O_2 and H_2O among other gases in the atmosphere. When the proton beam interacts with the moist atmosphere of the target area, it will lead to radiolysis of the present gases. The radical production may lead to the formation of oxidizing agents such as hydrogen peroxide and nitric acid. The presence of oxidizing agents may have a corrosive effect on the equipment, including the luminescent coating [6]. Therefore, the chosen material requires a satisfactory corrosion resistivity.

- **Temperature dependence** - When the high-power proton beam passes through a material, it will deposit energy which partly converts into heat, leading to increased temperature of the material [7]. Despite the planned cooling system for the proton beam window and target wheel at ESS, the bombarded materials are expected to reach temperatures up to 200 °C locally. The proposed luminescent coating has to have sufficient thermo-mechanical resistance but also satisfactory luminescent properties over the temperature range from room temperature to 200 °C [8].
- **Compatibility with thermal spraying** - The size and geometry of the target wheel limit the possibilities for applying the luminescent coating. It has been decided at ESS that the luminescent material will be spray-coated onto the target wheel and the proton beam window with flame spraying, a technique that is described in detail in Section 2.4 [9].

The spray coating used at SNS for PBI showed somewhat satisfactory results in terms of meeting the requirements. However, the manufacturer has stopped producing the precursor material, which eliminates the possibility of continuing to use the same material. As the recipes are not publicly available, efforts have been made from ESS and SNS to determine the constituents and the manufacturing process, which is further discussed in Section 2.2. ESS collaborates with SNS, University West in Trollhättan and the University of Oslo in a search to find a new material that meets the high requirements of PBI at ESS. Being able to ensure that the multi-million EUR equipment is not damaged by the proton beam puts this challenge as a high priority, which is the motivation for this master thesis. In order to find the optimal material for this challenging application, the need to gain insight in and map the chemical, thermal and structural behavior of potential luminescent coatings is evident.

1.3 Scope

This master thesis aims to investigate and optimize luminescent materials for proton beam imaging at ESS. Among the many requirements for this challenging application, brightness is one of the most important. Therefore, the materials in this study are evaluated predominantly on their luminescent performance measured with photoluminesence spectroscopy. The study consists of three parts:

- **Part 1** The first part focuses on characterizing sprayed luminescent coatings made in earlier research. A selection of the given samples was chosen to evaluate how coating thickness and spraying technique affect the luminescent properties.
- **Part 2** The second part is the investigation and optimization of a new Cr-doped alumina precursor for thermal spraying. This material is the starting point in the development of finding a luminescent material for the PBI system at ESS. The study investigates the influence of synthesis route, annealing temperature, dopant concentration, particle size and ball milling on the luminescence of the powders. A recipe for a suitable synthesis route and post-synthesis treatment is studied in preparation for flame spraying.
- **Part 3** Certain limitations of the chromium doped alumina powder has created a great interest in investigating alternative luminescent materials for proton beam imaging at ESS. As the last part of this study, two alternatives; titanium doped alumina and cerium doped Yttrium-Aluminum-Garnet (YAG), are synthesized and evaluated as potential luminescent precursors for proton beam imaging at ESS.

All materials are evaluated with photoluminescence spectroscopy to determine their brightness. To understand the nature of the luminescent behavior, several analysis methods are included in this report, with a focus on X-ray Diffraction (XRD) and Scanning Electron Microscope (SEM). Due to the long list of requirements on the luminescent material, which will be detailed in Section 1.2, some topics are left out of the scope of this report. The temperature dependence of the luminescence, radiation resistance and corrosive resistance are not included in this report and will be handled in future studies.

2 Theory

2.1 Luminescence

A luminescent material is characterized by its property to spontaneously emit light after absorbing energy. When absorbing heat at high temperatures, the material will spontaneously emit infrared radiation, called incandescence [10]. These high temperatures at which incandescence occurs distinguish incandescence from luminescence. There are different types of luminescence and they are classified depending on how the excitation of electrons in a material occurs. In Photoluminescence (PL), electrons are excited by electromagnetic radiation, such as visible light, Ultra-Violet (UV) light or X-rays. An electric voltage induces Electroluminescence (EL), and an electron beam causes Cathodoluminescence (CL). At ESS, accelerated high-energy protons strike the proton beam window followed by the target wheel. By covering the proton beam window and target wheel with a luminescent material, the protons can induce Ionoluminescence (IL).

There is a wide range of materials that have luminescent properties. Commonly, the material is an inorganic solid forming a host lattice doped with a luminescent ion creating a luminescent center.

2.1.1 Luminescent centers

It is challenging to form a raw material completely without any impurities and extrinsic defects. Some of the defects have the property of absorbing and emitting light causing luminescence. When intentionally introducing impurities in the host lattice by doping a material, the crystallographic order is perturbed due to the size difference or differences in oxidation state between the dopants and the atoms in the host structure. The dopant is commonly an rare earth metal or transition metal such as Eu^{3+}, Cr^{3+}, or Ti^{4+} in the concentration range of 1 mol% homogenously distributed in the host lattice. Additional quantum states are formed, which result in other possible electron transitions. When a material is exposed to an energy source and the dopant, also called an activator, absorbs at least the excitation energy, an electron gets excited to the Lowest Unoccupied Molecular Orbital (LUMO). Eventually, it relaxes to the ground state again by emission of radiation. Not all materials show luminescence since some ions rather undergo nonradiative processes from the excited state back to the ground state. It could, for example, be in the form of an increase in the vibration of the host lattice. Nonradiative and radiative processes are competitive and there are different probabilities that they happen. The radiative emission needs to be predominant over the nonradiative process to make an efficient luminescent material [10], [11].

In the case of an anion defect, for example when an oxygen atom is missing, one or two electrons could fill the vacancy and be trapped by surrounding cations forming F^+- and F-centers respectively. These F-centers are also called color-centers and usually absorb light in the visible spectrum. The presence of F-centers can have a large impact on the optical and luminescent properties of a material. The production conditions, such as thermal annealing parameters, have an essential impact on the formation of F-centers. The defects can also originate as a result of irradiation of the material [12].

2.1.1.1 Crystal field theory

Even though the doping ion in the material usually gives rise to the luminescent property, the host lattice significantly impacts the emission. The positive metal ion interacts with the ligands and experiences a crystal field, an electric field from the neighboring atoms. The crystal field provides a change in the energy of d or f orbitals, resulting in an energy level splitting. In an octahedral symmetry, the dopant has six neighboring atoms. The electron field is causing the splitting of energy levels, which have been illustrated in Figure 4 so that the three orbitals d_{xy}, d_{yz}, d_{xz}, will decrease in energy, and d_{y^2}, $d_{x^2-y^2}$, will increase in energy. The three lower orbitals are referred to as t_{2g} and the two higher energy levels as e_g [13]. In a tetrahedral symmetry, the crystal field splitting appears so that the d_{xy}, d_{yz}, d_{xz} increase in energy and are referred to as e, and t2 orbitals: d_{y^2}, $d_{x^2-y^2}$ decreases in energy.

When an electron relaxes from an excited state, a photon emits with the energy corresponding to the energy difference of the orbital in the excited state and the ground state. In other words, an excess of energy during

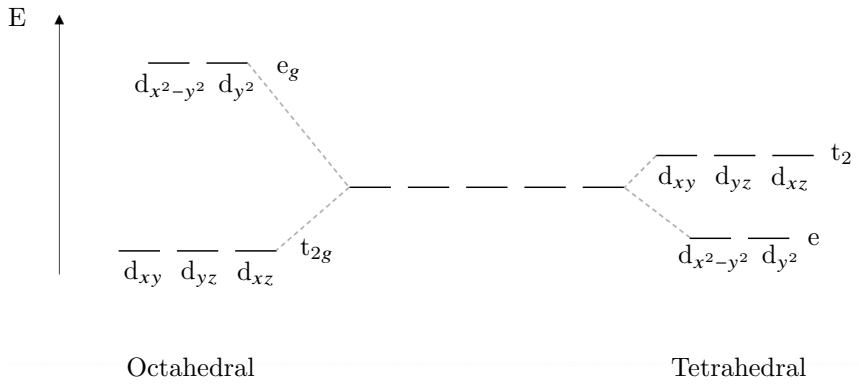

Figure 4: In an octahedral and tetrahedral complex the d orbitals of the metal ion split into two sets of energy levels due to crystal field.

absorption will not change the energy of the emitted photon. The wavelength of the emitted light is mainly in the visible range but also extends to the UV and infrared (IR) region. The excitation and relaxation are highly restricted by the electron configurations in the material and regulated by quantum mechanical laws. This results in some transitions being more likely to occur than others. There are mainly two different laws, the spin-selection rule and the so-called Laporte rule. The spin selection rule does not allow transitions where the total spin of the electron, S, changes, so $\Delta S=0$. The second rule, the Laporte rule, says that the change in angular quantum number Δl needs to be ± 1, which means an electron can only move between orbitals that differ in one quantum number and are not allowed to transfer to an orbital with the same quantum number. Some luminescent centers, such as transition metals, induce a broad emission band due to energy exchange with the surrounding atoms that undergo thermal movement/vibrations. On the other hand, rare earth metals will not be significantly affected by neighboring atoms due to the screening effects of electrons in their outer shell. In other words, sharp lines from well-defined electronic transitions will be shown in the emission spectra from these metals [14].

2.1.1.2 Luminescent lifetime

A transition that does not follow the spin-selection rule or the Laporte rule is called a forbidden transition. Despite its name, there is a small probability that the forbidden transition takes place, but it usually requires a longer time to fulfill. In a forbidden transition, the time the electron spends in the excited state is long and typically in the range of milliseconds. In contrast, the time for an allowed radiative transition is in the range of 10-100 nanoseconds. The average time an electron is in the excited state is called the luminescent lifetime [10], [15].

2.2 Luminescent materials

The vast number of materials that possess luminescence properties makes the quest of finding the optimal material for PBI immense, laborious and complex. To save time, money and effort, ESS has decided to continue on previous studies and chosen the material used at SNS as their benchmark material.

The material used at SNS is a chromium doped alumina coating, a ceramic material that is sprayed onto the desired places for proton beam imaging using the thermal spray pyrolysis method, a technique that is discussed in Section 2.4. The precursor that goes into the spray gun is a powder that is produced by the advanced material manufacturing company FJ Brodmann & Co. LLC. The powder will be referred to as the "Brodmann powder" in this report. The recipe of the powder has not been given out to ESS apart from the fact that it contains alumina and 1.5 wt% of chromia. The product is a fine powder with greenish-grey color. XRD is an analytical tool, discussed in Section 3.4.1, used to study the crystal structure of a sample. XRD

measurements were performed on the Brodmann powder and the results, seen in Figure 5, showed that the Brodmann powder contained Cr_2O_3 powder, which had been mixed with α-Al_2O_3 powder. By processing the XRD data, the amount of chromia was calculated to 1.5 wt%, which is in agreement with the specification from the manufacturer.

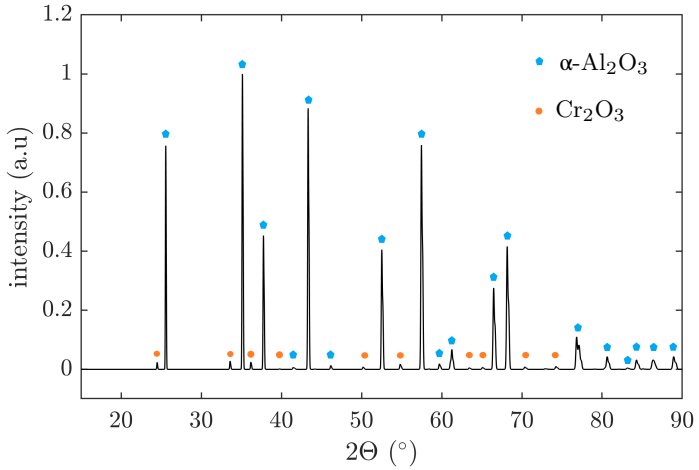

Figure 5: XRD data from the Brodmann powder. Peaks originating from Cr_2O_3 and α-Al_2O_3 are marked with orange dots and blue pentagons, respectively.

The results from the XRD measurement indicates that the incorporation of chromium into alumina takes place during the flame spraying, transforming the Cr_2O_3 and α-Al_2O_3 powder to chromium doped alumina.

Plasma-sprayed and flame-sprayed Cr-doped alumina samples have been given to ESS from SNS and University West, a university in Trollhättan that specializes on thermal spraying techniques. All samples given have been sprayed with the Brodmann powder as a precursor. The choice of sprayed samples are further detailed in Section 3.1, but their color range from greenish-grey to grey, depending on the spraying conditions. As a part of this thesis, a selection of the sprayed samples are characterized to determine how the luminescence is affected by various parameters.

2.3 Host material: Aluminum oxide

Aluminum oxide, or alumina is a ceramic material consisting of aluminum and oxygen with the stoichiometry Al_2O_3. It is cheap, abundant and has a high melting point at over 2000 °C. In comparison to other ceramics, it exhibits excellent chemical, thermal and physical properties. It is insoluble in water and organic solvents and shows low solubility in strong acids or alkalies. A major use of alumina is in the production of metallic aluminum, but it is also widely used as a chemical reagent or as pure alumina powder for various applications. There are various reported crystalline phases of alumina and they all have different properties in terms of mechanical properties, chemical stability and optical properties [16], [17].

The α-Al_2O_3 phase, also known as corundum, consists of Hexagonally Close-Packed (HCP) O^{2-} ions with Al^{3+} ions sitting in the octahedral voids of the structure, which is illustrated in Figure 6. To retain charge neutrality, only two-thirds of the octahedral sites are filled with Al^{3+} ions. α-Al_2O_3 is the most stable phase of alumina and has been used for many different applications, such as radiation dosimetry, insulation for nuclear reactors, mechanical parts for wear surfaces and host matrix in solid-state lasers [19].

Besides α-Al_2O_3, there are numerous other phases, such as $\delta, \theta, \kappa, \eta, \gamma$-$Al_2O_3$, that are so-called metastable structures of Al_2O_3. By heating aluminum hydroxides or aluminum salts, the material will transition through various structures. All transition phases eventually lead to α-Al_2O_3 at sufficiently high temperatures. The transition temperature from a metastable state into α-Al_2O_3 varies depending on the precursor, ranging from

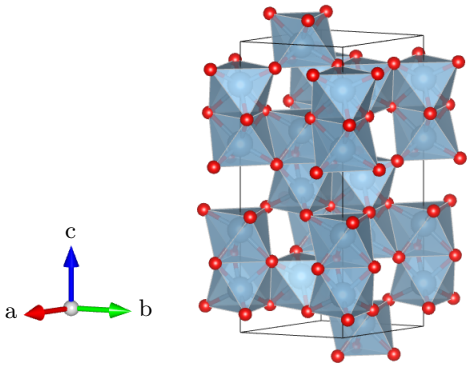

Figure 6: The unit cell of the corundum phase using a polyhedral model, where the small red dots are the oxygen atoms and the bigger balls in the octahedra are aluminum atoms. The image is created with VESTA software Ver. 3.5.3 with CIF. file provided by Tsirelson, V. G. et al. on Crystallographic Open Database [18].

600 - 1200 °C. Most transition phases crystallize in the spinel structure or a similar defect structure, with Face-Centred Cubic (FCC) O^{2-} with cations in tetrahedral voids and octahedral interstitial sites. The two transition phases η and γ are both a spinel but have varying ratios of cations sitting in tetrahedral sites and octahedral sites. 75% and 65% of the cations sit in octahedral sites for γ-Al_2O_3 and η-Al_2O_3, respectively [17].

2.3.1 Chromium doped Alumina - Cr-Al_2O_3

Over the past decades, transition metals have drawn attention within the field of luminescent materials. Transition metals have partly filled d-orbitals and usually form colored complexes. When doping α-Al_2O_3 with chromium(III) ions, the mineral ruby is formed, which gained interest quickly in the field of optical materials [10].

In 1960, Theodore H. Maiman at Hughes Research Laboratories invented the first functioning laser, using ruby as the lasing material, which established the modern laser technology. Ruby crystals are still central in the high-power lasers [20]. Chromium has several common oxidation states, +1, +2, +3, +4, +6, and the most stable form is +3. In ruby, the Cr^{3+} cation seizes the smaller Al^{3+} site surrounded by oxygen atoms. One thing worth mentioning is that pure Cr_2O_3 and Cr^{3+}-doped alumina have both octahedral crystal structures, although chromia (Cr_2O_3) is colored green and ruby red. The reason for the different colors is the crystal field strength that the Cr^{3+} ion is encountering. The crystal field strength variations on the Cr^{3+} ion are of high importance to the optical property of the material. In other words, a change in crystal field strength results in varying optical transitions with different energies, resulting in color variations [10].

The luminescent properties of Cr-doped alumina are well known. The luminescence mechanisms consists of three stages; excitation, non-radiative relaxation and radiative relaxation, which have been illustrated in Figure 7. The excitation can be stimulated by absorption of electromagnetic radiation. Cr-doped α-Al_2O_3 shows two broad absorption bands with peak positions in the ultraviolet and green light at around 400 nm and 553 nm, respectively [21].

After an electron is excited from the ground state to a higher energy state, it decays nonradiatively to the intermediate metastable state ^2E, where it further relaxes to the ground state $^4A_2$. This radiative $^2E \rightarrow {}^4A_2$ transition is characteristic of ruby and forms two sharp emission peaks, so-called R-lines. At room temperature, the first R-line is at 692.9 nm and the second at 694.3 nm, and the luminescent lifetime is 3 ms [22], [23]. It is worth mentioning that ESS desires a luminescent material with a shorter luminescent lifetime

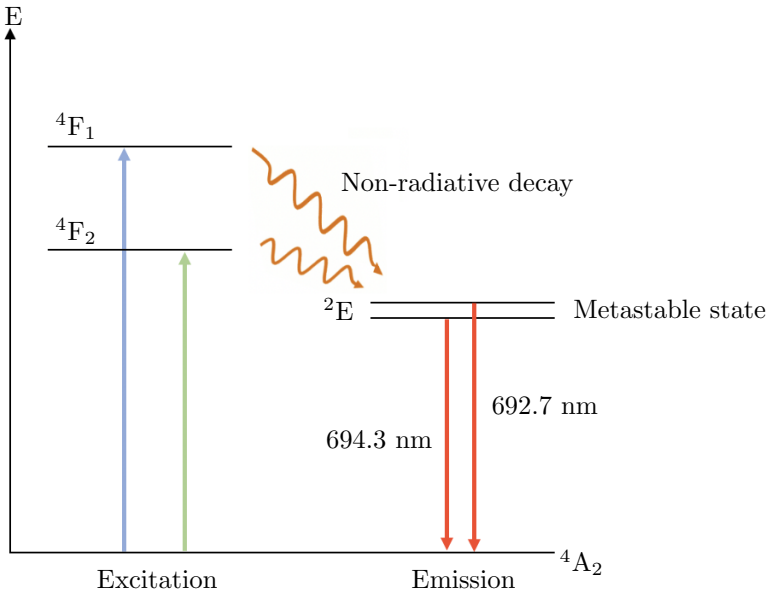

Figure 7: An energy level diagram showing luminescence mechanisms of Cr-doped α-Al_2O_3.

than 3 ms. The pulses of the proton beam will be 2.8 ms long, which makes 3 ms long luminescence lifetime very long in relation to the duration of the pulse. Studies have shown that the luminescence intensity of the Cr-doped η-alumina is significantly lower than ruby [11].

The doping concentration influence on luminescence has been extensively studied. The results on the optimal concentration of Cr^{3+} ions vary to some extent, usually in the range of a few wt% of Cr_2O_3, and are largely dependent on the synthesis methods and post-synthesis treatment used for the material. Therefore, the concentration dependency between the different studies might not be directly comparable. They all agree that when increasing the concentration above a certain level, the Cr^{3+} ions cannot fully be incorporated in the Al_2O_3 matrix, resulting in lower luminescence. An additional effect is concentration quenching, which happens when the concentration of the activators is high and energy transfers between the activators, resulting in a decrease of luminescence. On the other hand, at very low concentrations, fewer Cr^{3+} ions are present in the Al_2O_3 matrix resulting in fewer activators and fewer emitted photons, suggesting a balance of dopant ions give the optimal luminescent properties [21], [24], [25].

Cr-doped Al_2O_3 can be synthesized in several ways. An excellent solid-state ruby laser consists of a single crystal without any defects. There are mainly two methods to grow a ruby single-crystal, the so-called Verneuil and Czochralski processes [26]. The preparation of Cr-doped alumina powder samples differs from growing a single crystal of ruby. There is a variety of methods to produce luminescent Cr-doped Al_2O_3 powder and solid-state synthesis is a widely used method. In that method oxides are mixed before annealing in the furnace at a temperature over 1200 °C. The high temperature is needed to form the desirable α-alumina phase. Other methods worth mentioning are combustion synthesis, sol-gel method, detonation synthesis, hydrothermal and microwave solvothermal method [27], [28], [21], [29].

One of the requirements of the luminescent coating is, as mentioned earlier, a short luminescence lifetime. Since Cr-doped alumina has a luminescence lifetime in the range of milliseconds, it is of interest to find alternative materials with a shorter luminescence lifetime. The following section will therefore focus on two potential materials, which from the literature, have a significantly shorter luminescence lifetime. Additionally, the materials may also show brighter luminescence.

2.3.2 Titanium doped Alumina - Ti-Al_2O_3

Another luminescent transition metal-doped material is titanium doped alumina. The first operation of Ti-Al_2O_3 lasers was reported at the Twelfth International Quantum Electronics Conference in Munich in June 1982 [30]. Since then, Ti-doped alumina has been used for highly advanced technological applications, such as radiation dosimetry and scintillation detection and more[31], [32].

One more prominent feature that gives Ti-doped Al_2O_3 considerable attention is its broad emission spread ranging from the ultraviolet to the near-infrared region. The underlying mechanisms behind the different emission spectra of Ti-doped Al_2O_3 have been extensively investigated. Despite the great number of studies on the subject, researchers have not yet fully understood the complex nature of Ti-doped alumina luminescence. However, several hypotheses have been proposed, and it has been established that the oxidation state of the doped titanium ions in Al_2O_3 crystal (Ti^{3+} and Ti^{4+}) has a large influence on the luminescent properties of the material [33], [34], [32].

The material has been used dominantly for two different types of lasers: near-infrared lasers and blue lasers. The near-infrared emission band ranges between 670-1070 nm, with its peak at 800 nm. It has been demonstrated that the red emission spectra origins from ${}^2e_g \rightarrow {}^2t_{2g}$ transitions of the Ti^{3+} cations. The corresponding absorption occurs in the visible blue-green spectra around 400-600 nm. The emission and absorption bands are widely separated, which is seen in Figure 8. This due to the vibrational coupling of the Ti^{3+} cation and the alumina lattice. As can be seen in Figure 9, non-radiative transitions such as lattice vibrations introduce more possible electron energy levels. This leads to an increase in the number of possible excitation and radiative relaxation transitions and hence, broadens the band of the luminescence spectra [35].

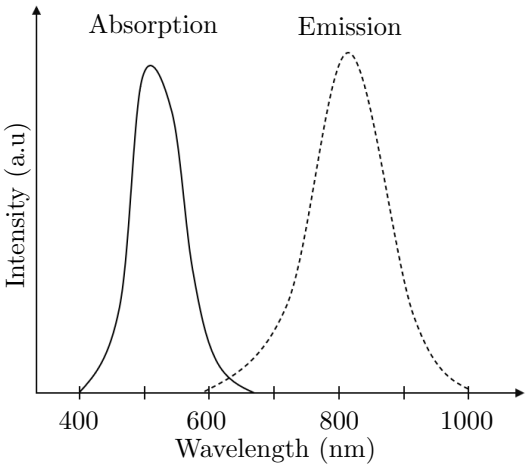

Figure 8: Ti-doped alumina red laser luminescence spectra.

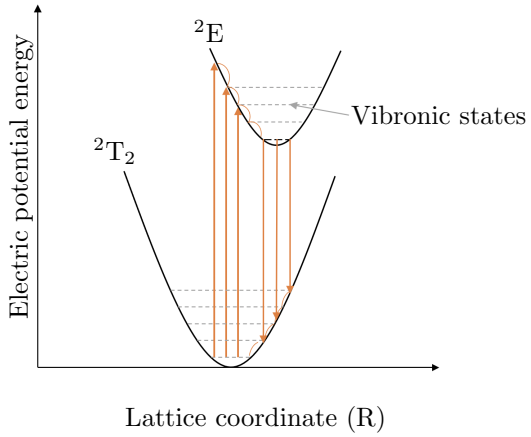

Figure 9: Energy diagram of Ti-doped alumina.

In contrast to the red emission, whose origin is well understood, there is much ambiguity regarding the origin of the blue emission of titanium doped alumina. Several hypotheses have been proposed on the underlying mechanisms of the blue emission around 420 nm, and while many studies connect the emission to the presence of Ti^{4+} ions in the crystal, recent studies have proposed the mechanism is of complex nature and require both Ti^{4+} ions and F-centers [32], [36].

There are several ways to produce luminescent titanium doped alumina, but the majority is produced as single crystal Ti-Al_2O_3. Among the different methods to synthesize Ti-doped alumina crystals is the Czochralski method one of the most commonly used. The technique is based on melting the feed material in a crucible at

very high temperatures. A spinning single-crystal seed is lowered onto the surface of the feed melt, causing the crystal seed to grow on the surface of the melt. Then, the single crystal is slowly pulled out of the feed melt which solidifies the interface and a crystal is grown [37].

Contrary to single-crystal alumina, the research on the luminescent properties of titanium doped polycrystalline alumina is limited. One publication demonstrates the luminescence of titanium doped η-Al_2O_3 powders produced with co-precipitation of alumina and titanium salts. The powder was heat treated at 600 °C in a H_2 atmosphere. The produced material exhibited luminescence but with very low intensity in comparison to single crystal Ti-Al_2O_3 [38].

The synthesis and post-treatment conditions also have an impact on the luminescence of Ti-doped alumina [34], [39], [38]. By letting the synthesis or sintering of a material take place in a reducing or oxidizing environment, the ratio of Ti^{4+} to Ti^{3+} ions can be altered in the finished material. The reducing environment is usually hydrogen gas, often mixed with an inert gas, which has been concluded to increase the amount of Ti^{3+} in an alumina crystal [40]. Oppositely, synthesis or post-synthesis annealing taking place in an oxidizing environment, often oxygen gas, will transform Ti^{3+} to Ti^{4+} ions. Thermal annealing in an oxidizing environment also introduces an excess of O^{2-} ions that contribute to charge neutrality when tetravalent titanium ions are present in the structure [41].

The doping concentration of titanium in alumina is generally low and can range from only a few ppm to 0.1 wt %. As already stated, the luminescent properties are strongly dependent on many variables including for example synthesis method, thermal treatment, experimental set-up for luminescence measurements. Therefore, it is difficult to draw any conclusions regarding the influence of doping concentration by comparing results on luminescence from different sources. Mikhailik et al. studied the titanium concentration dependencies in the luminescence of Ti-Al_2O_3. In this study, it is clearly shown that not only does the intensity change with concentration, but also the entire luminescence spectra.

Temperature also affects the luminescence spectra of the Ti-doped alumina in various ways. Several studies have reported how the intensity and position of the red emission peak has shifted with increasing temperature [42]. Some peaks have shown to even disappear at certain temperatures [32]. Another temperature dependent property of titanium doped alumina is the luminescence lifetime. Ti-doped alumina has a luminescence lifetime in the range of microseconds, which decreases with increasing temperature. According to Powell et al. the blue emission and red emission have fluorescence lifetimes of 23 µs and 3 µs at room temperature, respectively [34]. A short luminescent lifetime is a desirable feature of luminescent coatings for the PBI system, as it reduces the streak effect that is discussed in Section 1.2.

2.3.3 Rare earth doped yttrium aluminum garnet

Another host material that has attracted considerable attention in the solid-state laser industry is the YAG, which is widely used due to its great mechanical properties, thermal stability and radiation resistance [43]. The unit formula of YAG is $Y_3Al_5O_12$ and its unit cell, which is shown in Figure 10, consists of four formula units with a single type of Y-site. Eight oxygen ions surround every yttrium ion in a distorted decahedron constellation and the aluminum ions sit in octahedral sites [44]. The highly isotropic nature of the crystal structure facilitates controlled fabrication in a manner that yields crystals with great optical properties and transparency. As for the case of Al_2O_3, introducing small amounts of impurities into the host matrix can give YAG luminescent properties. Rare earth metals are natural dopant candidates for two reasons: they have similar ionic radii to yttrium, the host atom that is substituted by the dopant, which is a prerequisite for the dopant to be adapted into the structure. Secondly, rare earth metals possess a wealth of sharp fluorescence transitions representing most parts of the visible and near-infrared spectrum. The fluorescence spectra arise from electron transitions of partly filled $4f$-orbitals. Due to strong shielding from $5s$ and $5p$ shells, the rare earth luminescence is typically very narrow and only varies slightly in different host matrices [45].

The majority of all rare earth metals have been investigated as dopants on YAG and many of them have shown to be successfully luminescent (Nd^{3+}, Er^{3+}, Tm^{3+}, Ce^{3+}, Sm^{3+}, Ho^{3+}, Yb^{3+}, etc.) [45]. Ce:YAG is one

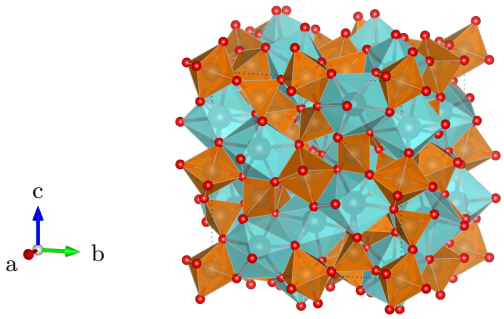

Figure 10: The unit cell of YAG. The red dots are oxygen ions, the yttrium ions sits in the teal dodecahedral voids, and the aluminum ions sits in the orange octahedra. Image is created with VESTA software 3.5.3 with CIF. file provided by Nakatsuka, A, and Yoshiasa, A. and Yamanaka, T. on Crystallography Open Database [44].

of the most popular doped YAG materials, which plays an important role in white Light Emitting Diodes (LED), for electron detection in scanning electron microscopes and X-ray and γ-detection in scintillator fields. It is commonly known for its very bright luminescence with high quantum efficiency and good light yield (photons emitted per energy deposited in the material by an energy source). One of the more advantageous features of Ce:YAG for luminescence screen for PBI at ESS is the short luminescence lifetime, which is measured to be in the nanosecond range and decreases with increasing temperature [46], [47]. According to the literature, the emission of Ce:YAG consists of two peaks, one in the UV region and one broad ranging in the green and yellow region (with a maximum around 525 nm) [48]. The origin of these two peaks is electronic transitions of the lowest excited states of $5d$ ($5d_1$, $5d_2$) to the ground-state of $4f$ levels. However, the UV emission is only present at low temperatures and is negligible at room temperature [49]. Ce:YAG can be excited either by UV around 260 nm and in the blue region around 460 nm [48].

One concern with cerium doped YAG is the so-called luminescence quenching. Quenching is observed in many luminescent materials and is caused by mechanisms that allow electrons in an excited state to relax to their ground-state via an alternative nonradiative route. The nonradiative mechanisms, proposed to be phonon generation (lattice vibration) or defect re-combinations, compete with the radiative relaxations and therefore limit the performance of the luminescence. Quenching is thermally activated and usually and a more significant impact at higher temperatures. The onset temperature, the temperature at which the quenching begins to affect the luminescence, also changes with dopant concentration. For YAG:Ce with doping levels below 1%, have their onset temperature at 600K while the quenching starts at 400K once the doping concentration reaches 1% [50]. This can be an issue since the target wheel is expected to operate between room temperature up to 200 °C (approximately 573K), as mentioned in Section 1.2.

Various ways of synthesizing luminescent Ce:doped YAG have been reported over the years. Commonly used methods include solid-state reaction, solution synthesis and co-precipitation. Thermal spray pyrolysis has also been shown to produce luminescence doped YAG, which is the planned synthesis for the luminescent coating at ESS. However, in order to achieve brighter materials with flame spray pyrolysis, the powders have to be treated with post-synthesis heat treatment to increase the crystallinity [51]. Similar to the titanium ions in Al_2O_3, there is a natural occurrence of both trivalent and tetravalent cerium ions in YAG. The trivalent cerium ions are responsible for the characteristic luminescence around 525 nm while the Ce^{4+}, or CeO_2, has no optical transition in the yellow-green region of the visible spectra. The post-synthesis annealing environment can change the ratio of Ce^{3+}/Ce^{4+} in the material, and by annealing in inert gas mixed with hydrogen gas environment it prevents oxidation of Ce^{4+} to Ce^{3+}.

2.4 Thermal spraying pyrolysis

Thermal spraying pyrolysis includes a range of different sample preparation methods in which fine particles of molten, semi-molten or even solid materials are deposited onto a surface to form a coating, which is illustrated in Figure 11. In the spraying process, the precursor material is heated by an energy source and accelerated onto a substrate on which the particles cool down, flatten and solidify. Both metals as well as non-metallic materials, such as ceramics, are suitable materials for thermal spraying processes. Various forms of precursors are used for thermal spraying coating techniques, such as powders, solutions and suspensions. It depend greatly on the technique used. Among the wide variety of techniques are flame spraying and plasma spraying.

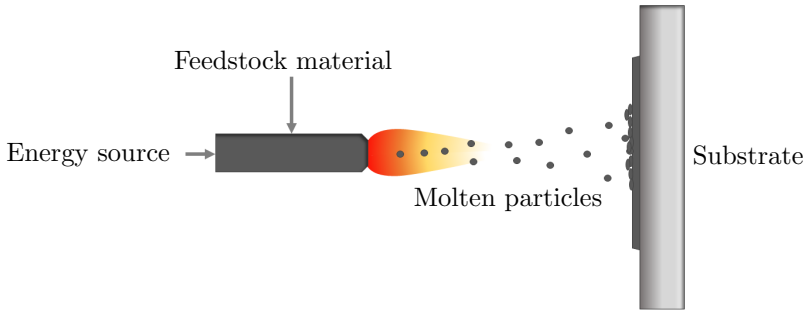

Figure 11: A schematic image of thermal spraying pyrolysis.

Flame spraying is one of the oldest, though still an extensively used thermal spray coating technique. In this technique, the energy created by the combustion of fuel gases is used to heat the feedstock material. Fuel gases can reach temperatures above 3000 °C upon combustion with oxygen, creating a high-temperature flame. The precursors are led by a gas inlet via a nozzle to the flame. Once the particles reach the flame they melt and accelerate towards the substrate [52]. Flame spraying is known for producing coatings of inferior qualities, e.g lower density coatings, in comparison to other techniques, but is cheap and easy to operate [53].

Plasma spraying is spraying technique that reaches extremely high torch temperatures. Instead of using the chemical energy of fuels, this spraying method utilizes the heat generated from plasma. Plasma, known as the fourth state of matter, is created when a large amount of energy is transferred to gases until the gas molecules atomize or monatomic gases ionize. A strong electric field can sustain the plasma, but as soon as the electric field is removed, the plasma re-combines into gas molecules again, generating large amounts of heat. For flame spraying, the precursor is transferred with a gas flow into the gun nozzle where an electric arc discharge heats the gas until a plasma is formed. As the plasma leaves the outlet of the nozzle and returns to the gas state, the temperature can reach up to 12000 - 16000 °C, making plasma spraying a suitable coating method for precursors with a high melting point [52].

Plasma spraying and flame spraying can produce materials with various properties and functionalities. These are therefore suitable techniques for a vast number of applications. Using thermal spraying for luminescent coatings has not only been attempted at SNS, but several publications have shown optical and luminescent properties of coatings produced with the same methods [54], [55]. Regarding the high tunability of the coating process, a number of parameters affect the properties of the sprayed coating. University West has in collaboration with ESS optimized spraying parameters for luminescent coatings using the Brodmann chromia-alumina powder that was used at SNS. Some of the parameters that have been optimized are gas flow rates, types of fuel, torch temperature, coating thickness and particle size of the precursor powder.

From their studies of spraying with powder precursors, particle sizes between 5-60 µm found to produce the most satisfactory results.

In general, it has been demonstrated that particle size and crystallite size affect the luminescence properties of powders. Larger crystal size is correlated with stronger luminescence as larger crystals significantly decrease the defect density, counteracting the quenching effect that defects have on the luminescence. Similarly, the particle size can also affect the density of defects, but it has been shown to have a less pronounced effect on the luminescence in comparison to crystal size [56].

3 Method and experimental part

3.1 Sprayed samples

In earlier studies, different spraying parameters and techniques have been investigated. With the Brodmann powder as the precursor, University West has produced 30 sprayed samples that have been provided to ESS for characterization. The samples are of varying coating thickness, produced by different spraying techniques and with different spraying parameters. Out of the 30 samples, 5 samples were selected for investigation to understand how the crystal structure and morphology of the sprayed coatings are correlated with their luminescent properties. Also, the impact on coating thickness and spraying techniques on luminescence was tested. Images of the samples can be seen in Figure 12 and the samples are listed below.

- Flame sprayed sample from University West (thickness of 50 µm, 100 µm, 200 µm, 300 µm)
- Plasma sprayed sample from University West (thickness of 200 µm)

(a) (b)

Figure 12: Images of the spray coated samples where a) flame sprayed and b) plasma sprayed sample from University West. The colors of the plates are, as seen in the figure, greenish-grey and grey respectively.

3.2 Preparation of new Cr-doped alumina precursor

As for the case of the "Brodmann powder", the chromia and alumina react during the spray pyrolysis. The idea of synthesizing a new chromium doped alumina precursor material is to produce a luminescence precursor prior to flame spraying. The doping of the Cr^{3+}-ions in the alumina phase was achieved with two different synthesis methods; solid-state and solution-based synthesis.

3.2.1 Cr-doped alumina - Solution-based synthesis

The solution-based synthesis is a thermal decomposition method where precursors are dissolved in an appropriate solvent [57]. In the preparation of Cr-doped alumina samples with the solution-based method, the precursor used were aluminum(III) nitrate nonahydrate $Al(NO_3)_3 \cdot 9H_2O$ (98.5%, Emsure) and chromium(III) nitrate nonahydrate $Cr(NO_3)_3 \cdot 9H_2O$ (98.5%, Alfa Aesar). The amounts corresponding to 1.5 wt% Cr_2O_3 (0.51 mol%) of the starting materials were weighted up and dissolved in water under magnetic stirring. The solution was then heated on a heating plate to evaporate the water, after which the temperature was further increased to release nitrogen oxides, see the net reaction formula in Equation 1. Once the water and NO_X gases were evaporated, the solution turned into a yellow spumous solid, which was then ground with a mortar and pestle before sintering in furnace at 1100 °C and 1550 °C for 8 h, respectively.

$$2\,[Cr(NO_3)_3 \cdot 9\,H_2O] + 2\,[Al(NO_3)_3 \cdot 9\,H_2O] \longrightarrow Cr_2O_3 + Al_2O_3 + 12\,NO_{2.5} + 72\,H_2O \quad (1)$$

The standard amount was 1 g of finished Cr-doped alumina, which was prepared by mixing 7.28 g of $Al(NO_3)_3 \cdot 9H_2O$ (19.4 mmol) with 52.7 mg of $Al(NO_3)_3 \cdot 9H_2O$ (0.13 mmol).

3.2.2 Cr-doped alumina - Solid-state synthesis

The precursors in a solid-state synthesis are usually fine-grain oxide powders. The idea behind the solid-state synthesis is to mix powders and subject the mixture to high temperatures to allow the oxides to react. The rate of diffusion increases with temperature, which explains the required high temperatures to obtain full incorporation.

The preparation of Cr-doped alumina by the solid-state synthesis was done by mixing aluminum(III) oxide powder (99.98 %, Sigma Aldrich) and chromium(III) oxide powder (99 %, Alfa Aesar) in different quantities. Nine samples with concentrations ranging from 0.05 wt% to 2 wt% (0.017 mol% to 0.68 mol%) of Cr_2O_3 were prepared to find the optimal doping level that yielded the highest luminescent intensity. After mixing with a mortar and pestle, the powders were annealed in a furnace in the air atmosphere. Samples were sintered at three different temperatures 850, 1100 and 1550 °C for 8 h with a heating rate of 300 °C/h.

$$99\,Al_2O_3 + Cr_2O_3 \longrightarrow 100\,Cr_{0.02}Al_{1.98}O_3 (1\text{mol}\%) \tag{2}$$

3.2.3 Ball milling

Another method to homogenize the samples in addition to mortar and pestle is ball milling. When ball milling, the sample is placed in a closed container together with a number of stainless steel balls. The container is then attached to a holder that shakes the container with a set frequency for a period of time, during which the steel balls inside the container create frictional and impact force on the particles. Besides homogenizing, this process efficiently reduces the particle size. A laboratory ball mill 'Retscher Mixer Mill mm400', with a container and balls made of stainless steel, was used to investigate the ball milling effect on the properties of the finished sample. Approximately 1-2 g of powder was used per run and the number of steel balls was 10-12. The ball milling program used in this study was 20 Hz for 5 minutes.

3.2.4 Sieving

One of the requirements on the precursor that came from University West is the particle size. In order to produce coatings with optimal properties using flame spraying pyrolysis, they have concluded that the precursor particles in the size range of 5-60 µm yield satisfactory products, optimally between 10-45 µm. Powders were therefore sieved through shafts of fine-meshed sieves with varying mesh-sizes with the aid of a 'RETSCH Vibratory Sieve Shaker AS200 Basic'[58] to collect different particle sizes. To investigate the particle size dependency on the luminescence, the powders collected in the different shafts were measured with PL spectroscopy. The different mesh sizes used for sieving the powders were 63, 75, 105 and 125 µm.

3.2.5 Scale-up

The luminescent properties of the pre-sintered precursor are likely to be affected to some extent during flame spraying. To see the true performance of the pre-sintered precursor, it has to be flame sprayed. The amount of precursor required for pilot run is 1 kg. Therefore, the capability to produce larger amounts of the powder was investigated. The solid-state synthesis was used because of its simplicity and lower contamination risk. As mentioned earlier, the dopant concentration dependency on the luminescence of Cr-doped alumina was investigated. Once the optimal concentration was found the synthesis method was scaled up from 1 g to 1 kg. Due to the capacity of the sintering furnace, three batches with 350 g of finished powder in each were produced. The starting materials were Al_2O_3 (99.98 %, Sigma Aldrich) and 1 wt% (0.34 mol%) Cr_2O_3 (99 %, Alfa Aesar), resulting in 346.5 g of Al_2O_3 and 3.5 g Al_2O_3 in each batch. After mixing the starting materials with a mortar and pestle, the powder was sintered in air at 1550 °C with a hold up time of 8 h. The powder was then analyzed with XRD, XRF and PL spectroscopy to ensure successfully produced powder. Since the particle size is crucial for flame spraying, the particle size was controlled by sieving the powder with a sieve (mesh size 63 µm).

3.3 Preparation of alternative materials

3.3.1 Titanium doped alumina

The Ti-doped alumina was prepared with the solid-state method as well as a solution-based method. The samples from the solid-state synthesis were made by mixing aluminum(III) oxide powder (99.98 %, Sigma-Aldrich) with titanium oxide. Both the thermodynamically stable titanium(IV) oxide rutile phase (99.9%, Sigma-Aldrich) and the metastable anatase phase (99.7%, Sigma-Aldrich) were tested separately. Since none of the prepared samples showed any luminescence different combinations of TiO_2 (rutile) with acidic, basic respectively neutral activated aluminum oxide were also investigated. Samples with TiO_2 content ranging from 50 ppm to 6 wt% of TiO_2 were prepared to investigate how the doping concentration affected the luminescent properties. With the idea to get the Ti^{4+} ions more evenly distributed in the material and better incorporated, two solution-based synthesis were tested. Firstly, Aluminum(III) oxide powder (99.98 %, Sigma-Aldrich) were dispersed in isopropanol (≥ 99.8 %, Sigma-Aldrich) to form a slurry. The amount of titanium(IV) isopropoxide $Ti(OCH(CH_2)_2)$ (97 %, Sigma-Aldrich) corresponding to a given doping level in alumina was added to the slurry under vigorous stirring. After a few minutes, when the solution was well mixed, water was added and a rapid hydrolyzation of Titanium(IV) isopropoxide took place. A solvent screening was performed with 12ml/12ml, 12ml/24ml, 24ml/12ml and 24ml/24ml of isopropanol/water. 20 mmol of aluminum(III) isopropoxide was mixed with 0.18 mmol of titanium(IV) isopropoxide. The slurry was stirred for 24 h before the solid powder was separated from the liquid by vacuum filtering. To dry the samples even more before sintering, they were put in a vacuum furnace to remove all the remaining liquid. The dried powder was then sintered in air at 1550 °C for 8 h before it cooled down to room temperature. Secondly, aluminum(III) isopropoxide and titanium(IV) isopropoxide were dissolved in benzene and isopropanol, respectively. The benzene was the better alternative and 25 ml was added in a beaker. 5 ml of water was added to hydrolyze the aluminum(III) isopropoxide and titanium(IV) isopropoxide. To make sure everything hydrolyzes the solution was stirred over night before vacuum filtering, drying in a vacuum furnace and then sintering similarly to the other solution-based synthesis.

3.3.2 Cerium doped yttrium aluminium garnet

The method used for the preparation of Ce:YAG was a solution-based synthesis. Cerium(III) nitrate hexahydrate $Ce(NO_3)_3 \cdot 6H_2O$ (99 % Sigma Aldrich), aluminum(III) nitrate nonahydrate $Al(NO_3)_3 \cdot 9H_2O$ (98.5 %, Emsure) and yttrium(III) nitrate hexahydrate $Y(NO_3)_3 \cdot 6H_2O$ (99.8 % Sigma Aldrich) was used as starting materials. The nitrates were mixed and dissolved in water on a heating plate under vigorous stirring for 2 h. Thereafter, the temperature was increased to evaporate the water and NO_X gases. The spumous solid was then ground with a mortar and pestle before sintering in air at 1550 °C for 8 hours. A series of samples with different doping levels were prepared to investigate how the luminescence depends on the concentration of Ce^{3+} in the YAG garnet. The mole fraction of cerium in relation to YAG ranged from 0.03 to 5 mol%.

3.4 Characterization methods

3.4.1 X-ray powder diffraction

XRD is a powerful and non-destructive analysis method for characterizing all kinds of matter ranging from liquids to powders and crystals. The method is based on irradiating samples with an X-ray beam that interacts with the specimen due to its crystalline structure, giving information about atomic and molecular structures of crystals, phases and crystallinity. Crystals are ordered arrays of atoms, and X-rays are electromagnetic radiation that can be considered as waves. The wavelength of X-rays is in the same order of magnitude as the usual interatomic distance of crystals. The X-rays that travel through a crystalline material will constructively interfere with the sample if Bragg's law is satisfied:

$$n\lambda = 2d_{hkl} \sin\theta \tag{3}$$

The Bragg's law, shown in Equation 3, states that there is a relation between the interplanar spacings of the

unit cell (d_{hkl}), the wavelength of the monochromatic X-ray beam (λ) and the angle of diffraction in relation to the planes (θ), n is an integer, see the illustration in Figure 13 [59].

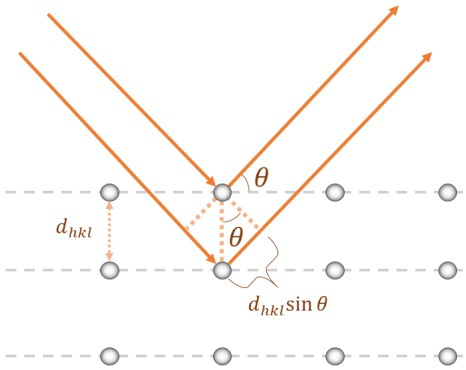

Figure 13: A schematic of diffraction following Bragg's law.

Powder X-Ray Diffraction (PXRD) is a diffraction technique used to characterize polycrystalline materials. The basics principles of the powder diffractometer consists of three main components; a X-ray source, a sample holder and a detector, as shown in Figure 14. The X-ray source is commonly a cathode ray tube. X-rays are passed through a monochromator to select one wavelength that is focused on the sample to make the interpretation of the results easier. To diminish the irregularities of the mounted sample, the sample holder spins around an axis (ω) in line with the X-ray beam. The detector collects all X-rays that have diffracted with a certain angle of 2θ relative to the path of the incident beam. During the course of measurement, the detector moves and collects X-rays over a range of angles 2θ. The result is a diffractogram of raw intensities of X-rays as a function of 2θ. It can be used to compare with data of already known crystal structures, similar to fingerprinting, but also to distinguish between amorphous and crystalline material and calculate the percentage of crystallinity and lattice spacing.

PXRD can be run in reflection mode, as seen in Figure 14, and transmission mode. Reflection mode is a convenient setting for the analysis of flat surfaces like solid plate samples. The geometry yields good intensity with high instrumental resolution. A drawback of reflection mode is the amount of sample required, which is an advantage with analyzing samples in transmission mode. With transmission mode, the collected X-rays have traveled through the specimen. The transmission mode is suitable when analyzing small amounts of powders. [60].

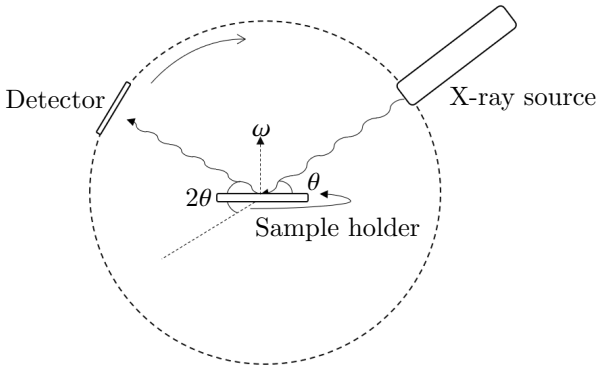

Figure 14: A schematic image of PXRD in reflection mode.

The XRD measurements in this study are performed with a Sore Stadi MP Seifert Analytical X-ray diffractometer equipped with a Dectris Mythen 1K detector and a Cu K_α source (40 kV, 40 mA) with a selected wavelength of 1.5406 Å using a (111)-germanium monochromator. Sprayed plate samples and powder samples were analyzed in reflection mode and transmission mode, respectively. For standard measurements, the selected step size was 0.255° with a counting time of 10 sec/step and the range of 2θ between 15-90 °. For more detailed measurements, the step size and counting time were 0.045 ° and 25 sec/step, respectively. A silicon wafer was used to calibrate the instrument. The samples were identified by comparison with crystallographic data of known phases obtained from the COD database [61]. Quantitative information was obtained analyzing the data with the Rietveld refinement in the software program GSAS-II (vers. 4782). For the preparation of the powder samples, a thin layer of powder was attached between two pieces of transparent tape and then put in the sample holder. Sprayed plate samples were mounted onto the sample holder with a piece of tack.

3.4.2 Scanning electron microscope

A Scanning Electron Microscopy (SEM) is an analytical tool that can record high-quality images of a sample with a resolution up to a few nanometers. The principles of the microscope are that an electron gun generates electrons with an energy of 0.1–30 keV. Lenses and apertures focus the electron beam before the electrons strike the sample. Scanning coils move the focused electron beam across the surface of the sample. In each position of the scanned area, different signals are generated from the interaction between electrons in the incident beam and the atoms in the sample [62].

A SEM is equipped with several detectors that collect the generated signal, such as backscattered and secondary electrons. The detected electrons can then form images containing complementary qualitative, quantitative and topographic information about the sample [63], [64], [65].

A SEM is also often equipped with an Energy-Dispersive X-ray Spectroscopy (EDS) detector. Ionization of an atom can happen when an incident beam electron collides with a core electron. After the ionization, the ion undergoes a relaxation when an electron, from an outer shell, fills the electron hole, and a characteristic X-ray is emitted. One thing to note going forward is that the energy difference between shells is well-defined and element-specific. Hence, qualitative and quantitative information of the atoms within the excitation volume can be obtained from the SEM-EDS technique. When the electron probe scans over the sample, emitted photons are recorded by an energy-dispersive spectrometer that records an energy spectrum. In other words, it is possible to form compositional maps of the sample [66].

The SEM used in this study is a high-resolution field emission scanning electron microscope, called JSM 6700F NT. It is located at the National Center for High-Resolution Electron Microscopy (nCHREM), hosted by the department of chemistry at Lund University. The accelerating voltage of the incident electron beam was set to 20 keV with a current of 20-50 µA.

3.4.3 X-ray fluorescence

Another non-destructive analysis technique is X-ray Fluorescence (XRF). The principles behind this multi-elemental analysis technique are based on the same as SEM-EDS. By measuring the energy/wavelength of the characteristic X-ray and the number of photons, a spectrum can be formed from which qualitative and quantitative information of the sample is obtained. The advantages of XRF are many. To mention a few, the sample can be in different states (powders, fluids and solids), it is fast and precise and the sample preparation is simple [59].

The XRF used in this study is a PANalytical MiniPal4 XRF Spectrometer located at ESS. A standard curve with different concentrations of Cr_2O_3 in alumina, ranging from 0-6 wt% was prepared. Approximately 1-2 grams of powder samples were put into a sample cup holder and then in the XRF spectrometer. From the standard curve, the intensity of the detected characteristic X-rays could then be recalculated to a corresponding concentration of Cr_2O_3.

3.4.4 Differential scanning calorimetry and thermogravimetry

Differential Scanning Calorimetry (DSC) is an analytical tool used to determine the thermophysical properties of a sample. The basic principle is to measure the amount of heat required to increase the temperature at a certain rate in relation to a reference. The change in heat flow can give information about physical transitions, such as phase transitions, or chemical reactions taking place in a sample as a function of temperature or time.

Thermogravimetry (TG) is an analysis method used to study the thermal properties of the materials. The basic principle of TG is to study the mass change of a specimen as a function of temperature. Physical and chemical phenomena such as vaporization, sublimation, absorption, desorption and decomposition can result in the mass change of a sample making TG a suitable analysis method to study such transitions.

In this study, both TG and DSC analysis were simultaneously performed with a NETZSCH STA 449 F3 Jupiter thermal analyzer. Appropriate amounts of sample ($\sim$ 10 mg) were put in an alumina crucible and weighed. The reference sample was an empty, identical sample crucible. Argon gas and nitrogen gas, with gas flows of 20 ml/min were passed through the sample environment to avoid undesired reactions from occurring. DSC and TG curves were then analyzed with NETSCH Proteus Thermal Analysis 8.0 software to determine transition temperatures and mass losses. Samples were analyzed with different temperature programs, with varying heating rates and end temperatures, to tailor the analysis for studying the phenomena of interest.

3.4.5 Photoluminescence measurements - Spectroscopy

When ESS is under operation, the luminescence from the sprayed coating on the target wheel and proton beam window will be induced by protons, which is called ionoluminescence. Ionoluminescence experiments require costly equipment that are only available on certain research facilities. For the case of simplicity, the luminescent properties of materials are, in this study, investigated with photoluminescence spectroscopy instead.

PL measurements were performed to evaluate the optical properties of the luminescent materials. There are several ways to measure the luminescence of materials, but UV-Vis luminescence spectroscopy is advantageous to do qualitative and quantitative analysis as it is efficient, cost-effective and easy to operate. Photo-excitation is expected to generate similar characteristic emission spectrum as proton-excitation, making it a suitable alternative analysis.

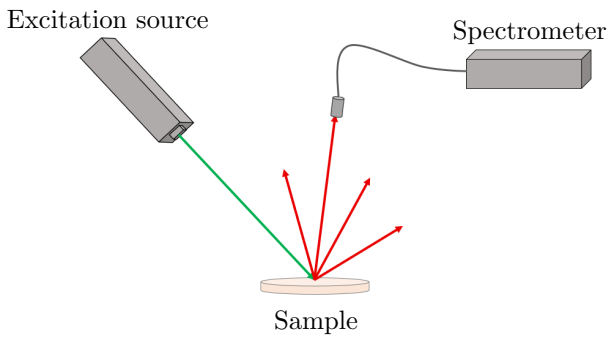

Figure 15: The set-up for luminescence measurements using a green laser as a excitation source.

Performing luminescence measurements requires two main components; an excitation source, and a spectrometer, which is illustrated in Figure 15. A laser is mounted so that the light is aimed at the sample. As the laser shines on the sample, photons will be absorbed by the specimen and re-emitted with another wavelength if the material is luminescent. An optical fiber collects and leads emitted and reflected photons to the spectrometer where the raw intensities at each wavelength are recorded. The result is a spectrogram

which shows the detected number of photons per second (cps) in a range of wavelengths. When using the same excitation source, the luminous intensity can be directly compared between different samples.

The thickness of the luminescent coating will have an impact on the light intensity from PL measurements, which can give misleading results of the measured photon yield when comparing two coatings with different thicknesses. This dependence is also expected to differ in comparison to the proton beam induced luminescence once ESS is in operation. A thicker coating can give off luminescence from deeper within the material and generate more photons. However, it will only generate more photons up to a certain point. Light intensity exponentially decays with penetration depth due to absorption. This depth is represented by the characteristic absorption coefficient α, which is inversely proportional to the distance that light with a certain wavelength travels in a specific material, called the absorption length. Another important factor is that the coating is sprayed onto an alumina or steel surface. The light that reaches the smooth surface of the substrate is reflected with the reflectance, R (a value between 0 and 1), which increases the photon density at a certain depth compared to a coating of equal thickness but without a reflective substrate. These two factors will influence both the excitation light and the emission light during PL measurements. A thickness normalization model created by C. Thomas has been further developed and evaluated in this study, see Appendix C. This model, and the theory behind it, suggests that the luminescent intensity asymptotically increases with thickness. The model, which has been fitted to earlier measurements performed at ESS, can be seen in Figure 39 in Appendix C [67]. The model is currently incomplete, which means that the results are not presented in this report but is taken into discussion when presenting the results of the luminescence coating thickness dependency.

Three different excitation sources were used in this study: a 525 nm green laser with 330 mA and two UV sources with wavelengths of 250 nm and 380 nm and a power of 100 mA and 500 mA, respectively. A spectrometer, product name "flame" from Oceanoptics, was used to collect the emitted light, the data was later analyzed with the software OceanView 1.6.7. Measurements were performed at room temperature. In order to assure that samples were measured under similar conditions, 0.4 g of powder was weighed and pressed into small cylindrical disks using a Laboratory pellet press GS15011 from Specac Ltd. When pressing, the weight applied for each pellet was four tonnes. A 0.5 wt% Cr-doped alumina pellet was used as a reference sample to adjust the aim of the optical cable and excitation source until a satisfactory intensity was obtained. Sprayed plate samples were directly measured without any sample preparation apart from height adjustment due to differences in aluminum plate thickness.

4 Results and Discussion

4.1 Sprayed samples

In this section, the results of the investigation on the sprayed samples are presented in two parts; the coating thickness dependence on the luminescence, and the effect that different spraying techniques have on the luminescent properties. In both of these sections, the discoveries on the morphological and crystallographic nature of the thermal-sprayed samples are also used to develop the new precursor for ESS.

4.1.1 Coating thickness

Three flame sprayed samples with identical spraying parameters but varying thickness (50 µm, 100 µm and 300 µm) were analyzed with XRD to study the effect of coating thickness on crystal structure.

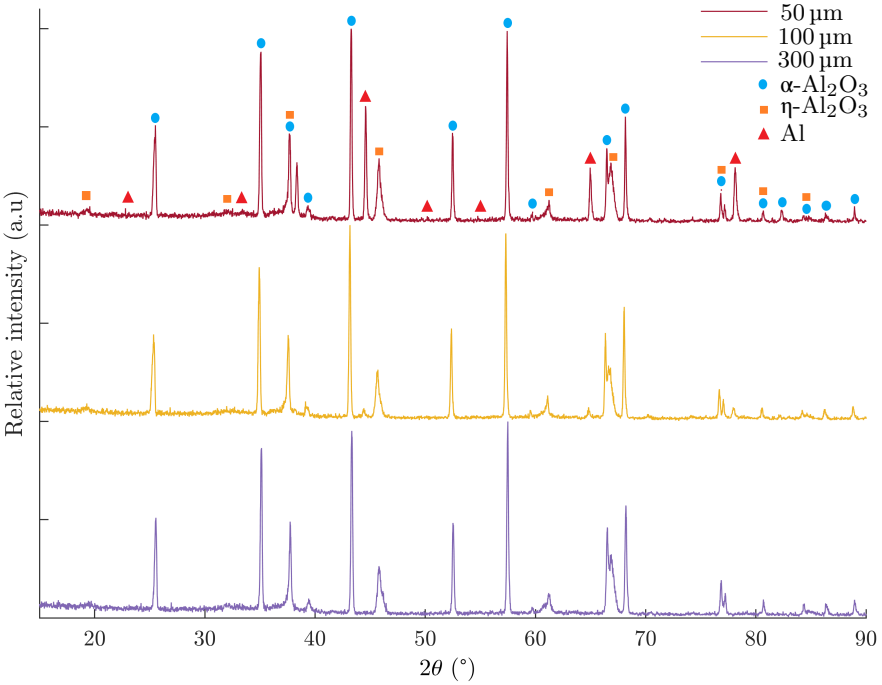

Figure 16: XRD patterns of flame sprayed samples with varying thickness 50 µm, 100 µm and 300 µm. The 50 µm sample is marked with phases in the samples. Blue circles, orange squares and red triangles mark the peaks corresponding to α-Al_2O_3, η-Al_2O_3 and aluminum, respectively.

Figure 16 presents the result of the XRD measurements. The three samples exhibit similar crystalline structures when observing the results, but differences can be noted. The dominant phase in every sample is α-Al_2O_3, marked with blue circles in the top diffractogram. The η-alumina is present in small fractions as well, marked with orange squares. Mentioned in Section 2.3.1, the Cr-doped η-alumina has been shown to exhibit inferior luminescence to Cr-doped α-Al_2O_3, which makes its presence in the coating undesired. The η-alumina seem to be present to the same degree in all three samples.

Aluminum peaks at 2θ = 38.5°, 44.6°, 64.9°, 78.1° and 82.3°, marked with red triangles, are present in the 50 µm pattern but not in the 300 µm sample. These peaks correspond to the aluminum substrate on which the coating is sprayed. There is a gradual disappearance of these peaks when comparing the 50 µm and the 100 µm patterns. 44.6°, 64.9° and 78.1° peaks are present in the 100 µm but in smaller fraction. As these samples are measured in reflection mode, fewer X-rays reach and reflect the substrate as the coating thickness increases. Beyond the presence of metal aluminum peaks on the 50 µm and 100 µm, the XRD

patterns vary to some extent in terms of the relative intensities of alumina peaks. Apart from the presence of aluminum in the thinner sprayed samples, the XRD patterns show that the crystal structures are rather similar.

4.1.1.1 Photoluminescence of coating thickness samples.

PL measurements were performed on 9 samples with four different thicknesses: 50 µm, 100 µm, 200 µm and 300 µm. Samples were excited with a monochromatic 525 nm green laser and the emission spectra were collected and integrated over 650-750 nm. The results are shown in Figure 17.

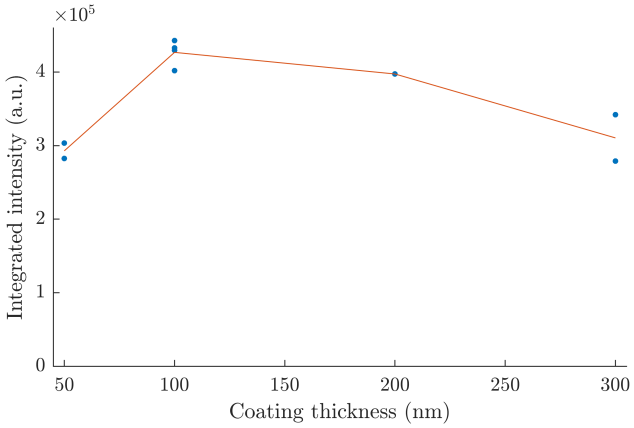

Figure 17: Luminescence measurements of flame sprayed samples with varying thickness where the integrated intensity between 650-750 nm is plotted against the thickness of the samples.

The luminescence intensities show that the optimal coating thickness is 100 µm. As previously mentioned in Section 3.4.5, the coating thickness will have an impact on the apparent luminescence. According to the theory presented, see Appendix C, the luminescence is expected to asymptotically increase with increasing thickness. This behavior is not observed in the measurements and instead 300 µm exhibits inferior luminescent intensity. The deviation could be explained with a few different hypotheses. One important thing to note is that the model and the theory that describes the asymptotic luminescence behavior as a function of coating thickness are currently incomplete and need further optimization. There might be mechanisms, not accounted for in the model, that result in a loss in luminescence intensity once coatings reach a certain thickness.

The lower intensity obtained from the 50 µm samples concurs with the theory of the model. The 300 µm sample is, however, more difficult to explain. A hypothesis is that upon thermal spraying, the molten particles form less of the α-alumina on a thick layer of coating relative to directly onto the aluminum substrate. Oriented surfaces could act as a nucleation site, similar to a seed, which could propagate the formation of a crystal phase, and increase the crystallinity of the coating close to the surface of the substrate. This effect could be lost as more coating is added on top, when spraying a thick layer. However, this speculation is not supported by the XRD measurements as crystallographic difference is not clearly visible on the XRD patterns. Due to the limited amount of samples, it is hard to draw any clear conclusions. The replicates, or samples with the same thickness, do also show to have slightly varying luminescent properties which means that the reproducibility of the flame spray process introduces some uncertainty to the analysis.

4.1.2 XRD of spraying techniques

This section presents how spraying techniques influence the luminescence and crystal structure of sprayed coatings. Figure 18 shows the XRD results of two selected plates: Plasma sprayed and flame sprayed plates from University West. To eliminate the error from the influence of coating thickness that is discussed in

4.1.1, samples were chosen with equal coating thickness (200 µm). The XRD pattern of the precursor, the Brodmann powder, is also added to the figure as a reference. The Brodmann powder consists of pure α-Al_2O_3 and Cr_2O_3 as earlier stated in Section 2.2. When comparing the XRD patterns with the precursor it is evident that the crystalline structure of the alumina phase has changed. While the α-Al_2O_3 is still present to a large extent, the η-Al_2O_3 contribution has increased to some degree both for the plasma sprayed and the flame sprayed samples. The relative intensities of the α- and the η-phase for the flame sprayed and the plasma sprayed sample reveal that there is a larger fraction of η-alumina in the flame sprayed than in the plasma sprayed, which can be seen most clearly on the peaks at 45.7°, 61.2°, 66.8°. This might seem intuitive as Al_2O_3 transitions into the α-Al_2O_3 at higher temperatures.

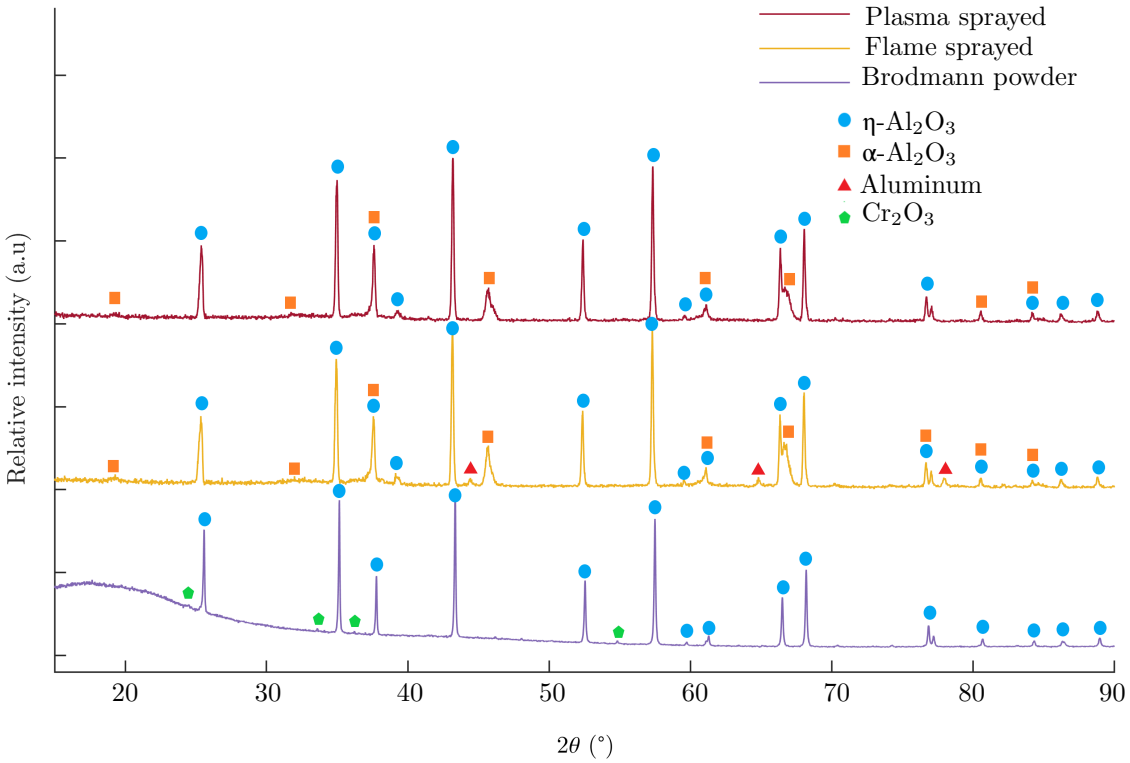

Figure 18: XRD patterns of the Brodmann precursor powder, flame sprayed and plasma sprayed samples from University West. The α-Al_2O_3 is marked with blue dots, the η-Al_2O_3 with orange squares, pure aluminum with red triangles and Cr_2O_3 with green pentagons.

However, the precursor consists of α-alumina, so one could argue that the torch temperature would have no effect on the formation of α-alumina. In fact, if the particles that pass through the torch do not completely melt, the solid core could act as a nucleation site for the formation of α-alumina. Following this reasoning could lead one to expect that not completely molten particles would favour the propagation of α-alumina in comparison to fully molten particles. If the particles fully melt in both spraying techniques, there would be no effect on the phase ratios from this factor. It is worth mentioning that the torch temperature is not the only factor that is different between the two spraying methods. Other factors might also influence the formation of the different phases. Plasma spraying is known to produce more dense materials than flame spraying, resulting in more material that can be excited and emit photons in the same thickness. Aluminum diffraction peaks are present in the flame sprayed sample but not in the plasma sprayed sample. This could be related to the lower density of the flame sprayed sample. The density difference is most likely to influence the luminescence, perhaps even to a larger extent than the differences in crystal structures.

The luminescent properties of the flame-sprayed and the plasma-sprayed samples are shown in Figure 19. Confirming with the discussion above, plasma spraying produces stronger luminescent coatings than flame spraying. Due to the lower amount of η-alumina and the knowledge that it produces denser material, it is expected that plasma spraying shows superior properties. However, ESS has chosen flame spraying as the method to produce the luminescent coating in the future, due to economical and practical reasons.

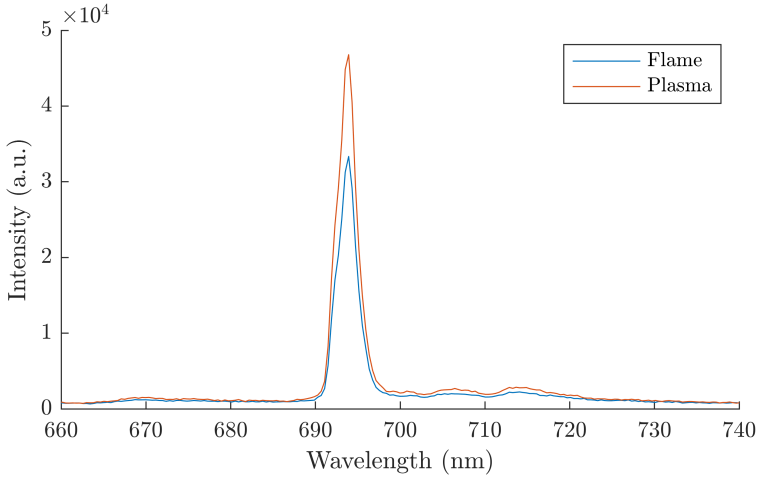

Figure 19: Photoluminescence measurements of flame sprayed and plasma sprayed samples.

SEM-EDS elemental mapping was performed on flame sprayed and plasma sprayed samples from the University West to investigate the presence of chromium particles. Figure 20a and 20b show SEM micrographs recorded by the secondary electron detector and the elemental maps from the same area of the samples are seen in Figure 20c and 20d. Chromium particles are distinguished both in the plasma-sprayed and flame-sprayed samples, which in other words means that the Cr^{3+}-ions are not fully incorporated in the alumina matrix. When spraying unreacted Cr_2O_3 and Al_2O_3, the doping of Cr^{3+}-ions in alumina structure takes place in the flame during a very short period of time, which introduces some uncertainties and could make the actual doping level difficult to control. This support the new precursor preparation method with sintering prior to flame spraying for a controlled and full incorporation.

4.2 Chromium doped alumina precursor

4.2.1 Structural evolution of the solid-state and the solution-based synthesis.

To understand the decomposition and phase transitions of the nitrates and oxides precursors, TG and DSC analysis were performed whose result can be seen in Figure 21. The starting material in the analysis in Figure 21a was $Al(NO_3)_3$ dissolved in water with $Cr(NO_3)_3$ with a concentration corresponding to 1.5 wt% Cr_2O_3. The water was evaporated prior to analysis. As one can see in the TG result, the nitrates show a continuous weight loss from approximately 200 °C to 500 °C, which can be derived from the evaporation of NO_X-gases. Above 500 °C there is no remarkable weight loss observed. Two exothermic peaks are found at 850 °C and 1150 °C, which suggest that the sample undergo crystallization forming the η-phase followed by a phase transition to α-phase (later confirmed with XRD measurements). TG and DSC graphs of Al_2O_3 mixed with Cr_2O_3 (1.5 wt%) are presented in Figure 21b. One thing to be noted about the TG result is that there is a small mass loss at above 1300 °C. To prepare Cr-doped alumina from aluminum oxide and chromium oxide, one would expect no weight loss since the oxides can not be thermally decomposed in this temperature range. Due to the high purity of the starting materials, the weight loss cannot be completely explained by impurities. Therefore, this measurement needs to be reapeted. When looking at the DSC curve, it exhibits an exothermic peak ranging from 850 - 1350 °C. The η and α-phase transition are indistinguishable but

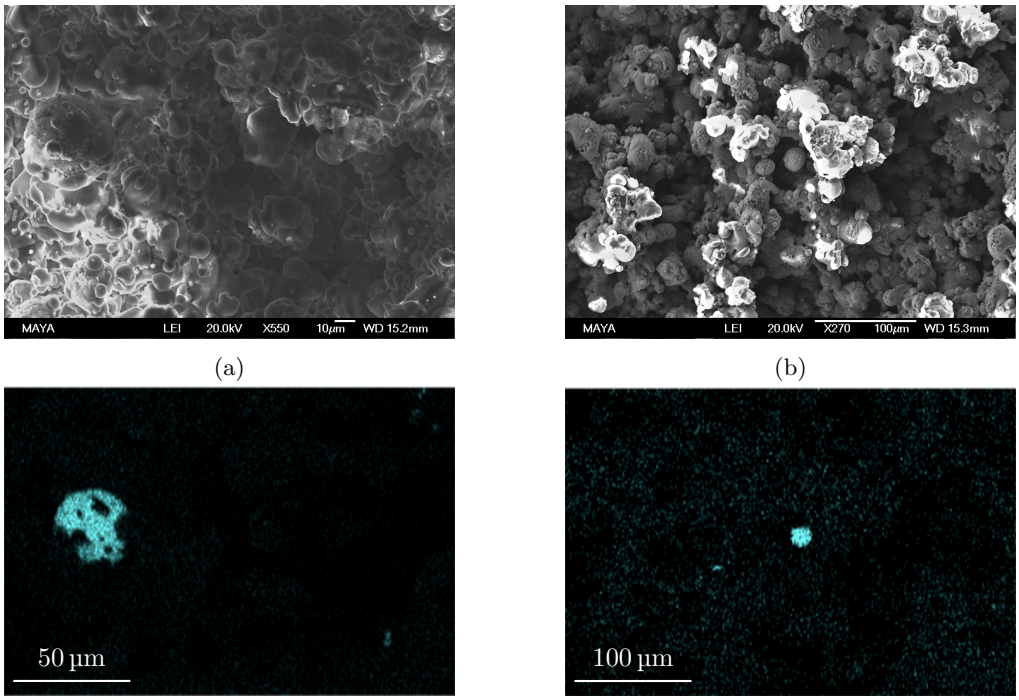

(a) (b) (c) (d)

Figure 20: SEM micrographs of a) plasma sprayed and b) flame sprayed samples with corresponding SEM-EDS chromium maps c) and d).

the large exothermic peak indicates the reaction between Al_2O_3 mixed with Cr_2O_3 and a gradual phase transition.

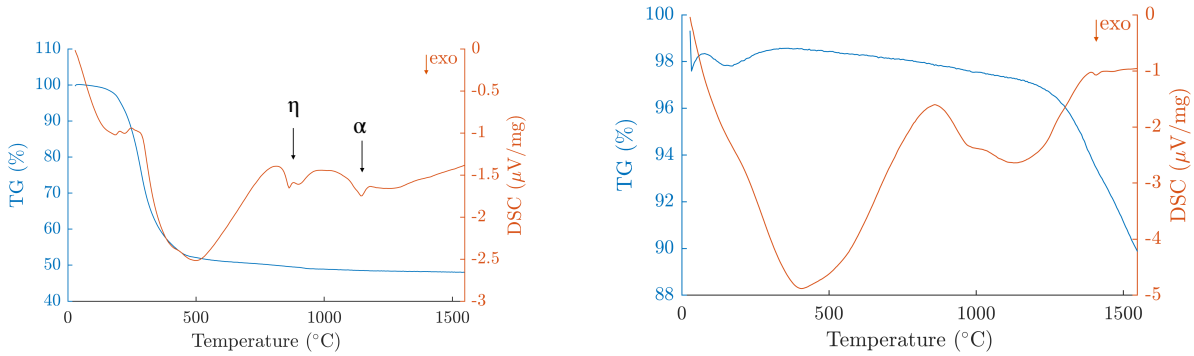

(a) (b)

Figure 21: TG and DSC measurements on a) $Al(NO_3)_3$ and $Cr(NO_3)_3$ and b) Al_2O_3 and Cr_2O_3 with a concentration equivalent to 1.5 wt% Cr_2O_3.

To investigate the structural evolution with temperature, samples sintered at different temperatures were analyzed with XRD. The sintering temperatures were decided based on the result of DSC measurements. For the solution based synthesis, the sintering temperatures were 600 °C, 850 °C and 1000 °C, whilst the sample prepared with solid-state method was sintered at 850 °C, 1100 °C and 1550 °C.

4.2.1.1 XRD - solution-based synthesis

Figure 22 shows the XRD patterns of 1.5 wt% Cr-doped Al_2O_3 synthesized by the solution-based method. The sample preparation and XRD analysis were performed at SNS. The result of the heat-treated sample at 600 °C indicates that the sample is amorphous. After sintering the sample at a temperature of 850 °C, broad peaks appear in the XRD pattern, which strengthens the argument that the exothermic peak at 850 °C in the DSC diagram originates from the crystallization of the sample. The 2θ-values of the broad peaks 32.1, 37.8, 37.9, 46.0, 46.1, 60.1 and 67.0 identify the crystalline phase as η structure even though it is predominantly amorphous. When increasing the sintering temperature to 1000 °C the XRD pattern shows that the crystallinity of the sample is enhanced since clear diffraction peaks are observed and the peak related to the spinel phase is not as distinct. By comparing diffraction patterns of possible phases, it can be confirmed that the sample heat-treated at 1000 °C contains predominant α-phase and to some degree η-phase. The sample annealed at 1000 °C was colored pink, which also supports successful incorporation of Cr^{3+}-ion in α-Al_2O_3.

One thing to note going forward is that the phase transition observed at 1150 °C in the DSC curve in Figure 21a may be derived from the η → α phase transition, but the XRD pattern of the sample sintered at 1000 °C already showed presence of α-phase. One explanation could be the fast heating rate in the DSC analysis. It can be seen that the exothermic peak begins near 1000 °C meaning the phase transition begins at that temperature. To clarify, the highest rate of the phase transition coincides at the maximum of the endothermic peak. However, the phase transition begins at lower temperatures suggesting that keeping the temperature at 1000 °C for a longer time will enable the α-phase transition.

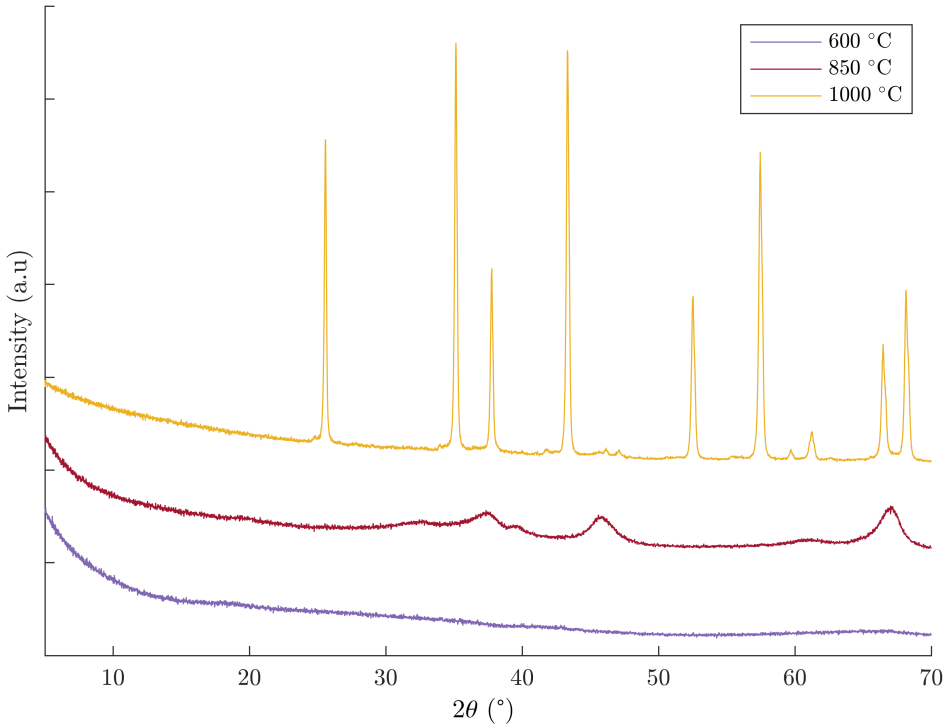

Figure 22: XRD pattern of solution-based 1.5 wt% Cr-doped Al_2O_3 sample that have been sintered at the 3 different temperatures 600 °C, 850 °C and 1000 °C.

4.2.1.2 XRD - solid-state synthesis

The result from the XRD analysis of 1.5 wt% Cr-doped Al_2O_3 prepared with solid-state method is presented in Figure 23. The XRD patterns of the sample sintered at 850 °C suggests an amorphous structure but the

small peaks at 37.8°, 46.0° and 67.1° indicate that a η-structure begins to appear. The sample annealed at 1100 °C shows clear diffraction peaks, which can be indexed to crystalline α-structure. A similar XRD pattern of the sample sintered at 1550 °C was observed, but the peaks were sharper. This can be an indication that the material sintered at 1550 °C has a larger crystallite size. The 1100 °C sintered sample is grey in color, while the sample sintered at 1550 °C is pink. This may be an indication that the phase transition from η to α-phase is not fully completed at 1100 °C.

When comparing solution-based with solid-state synthesized samples sintered at 850 °C, it can be seen that the peaks derived from the η-phase are less pronounced in the XRD pattern of the solid-state sample. This suggests that samples prepared by the solution-based synthesis enter the η-phase at lower temperatures compared to the solid-state synthesis.

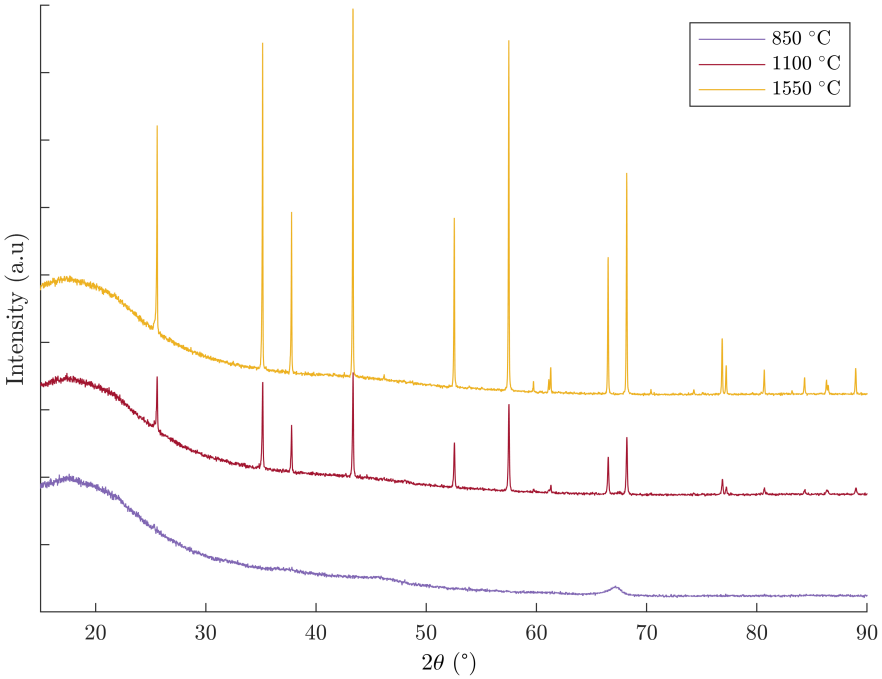

Figure 23: XRD pattern of solid-state synthesized Cr-doped alumina sintered at three different temperatures 850 °C, 1100 °C and 1550 °C.

4.2.2 Photoluminescence of solid-state synthesis vs. solution-based synthesis.

As mentioned in Section 3.4.5, the luminescence properties of the Cr-doped alumina samples were evaluated by recording a spectrum of photons emitted from green laser excitation. The different sintering programs (1100 °C for 8 h, 1300 °C for 2 h and 1550 °C for 8 h) and the two synthesis methods were evaluated. Figure 24a shows the result from PL measurements of the 1.5 wt% Cr-doped alumina synthesized with the two different methods and at the sintering temperatures 1100 °C and 1550 °C. The spectrograms show an emission peak at 693 nm, which corresponds to the characteristic ruby lines. This verifies the incorporation of Cr^{3+} ions in the Al^{3+}-sites in alumina. Since the resolution of the spectrometer is limited, only one peak is observed instead of two sharp R-lines. A broadband emission ranging from 670 nm to 720 nm can also be seen in the spectrogram.

It is shown that the emission intensity increases with sintering temperature. The synthesis method had an impact on the photoluminescent intensity for samples sintered at 1100 °C, where it was showed that the solid-state synthesis produced powders with far worse luminescent properties than the solution-based samples. As mentioned, the XRD pattern of Cr-doped alumina prepared by solution-based synthesis indicated that the

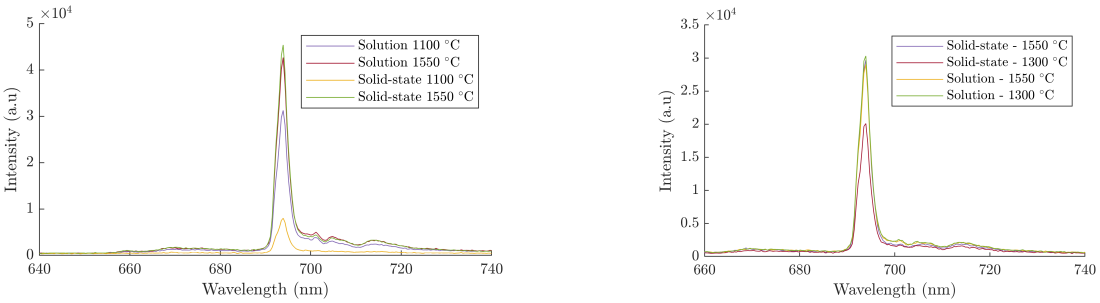

Figure 24: PL measurements of Cr-doped alumina powders, synthesized with the solid-state method and solution synthesis. The spectrogram in a) are from samples with 1.5 wt% Cr_2O_3 content, sintered with two different temperatures 1100 °C and 1550 °C for 8 h and b) are samples with a doping level of 1 wt% and sintered at 1300 °C for 2 h respectively 1550 °C for 8 h.

α-phase is the dominant phase already at 1000 °C. On the contrary, the sample prepared with the solid-state method (1100 °C) showed the presence of η and α-phase, which can explain the difference in luminescence intensity. The XRD patterns suggest that samples made of the solution-based synthesis enter the α-phase at lower temperatures compared to those made with the solid-state synthesis. During the heat treatment, the nitrates form complexes that are less thermodynamically stable compared to the oxide powders used in the solid-state method. Less thermodynamically stable complexes would require less thermal energy to undergo a phase transition. Samples sintered at 1550 °C, on the other hand, exhibited equally strong emission intensity, regardless of the synthesis method. A reason for the high PL intensity can be explained by the highly crystalline α-phases observed in both of the samples from the XRD patterns. BET-analysis, which is a method to determine the surface area of powders, was also performed on Cr-doped alumina after heat treatment at 1100 °C and 1550 °C, seen in Appendix B. Surface area is inversely correlated to particle size. A reduction in surface area was observed upon heat treatment from 1100 °C and 1550 °C, which suggests that the crystal size increases with sintering temperature. Crystal size also influences the brightness of a luminescent material, which is further investigated in Section 4.2.4.

In order to shorten the preparation time of the two synthesis methods and keep the good luminescent material, it was investigated how the sintering time and temperature affect the photoluminescent property of the samples. Two different sintering programs were used; the 1 wt% Cr_2O_3 Cr-doped alumina samples were heated from room temperature to 1300 °C respectively 1550 °C with a heating rate of 300 °C/h and hold up time of 2 h. Figure 24b presents the result from PL measurements and it can be seen that the luminescence of samples prepared with the solid-state (1550 °C), solution-based synthesis (1300 °C and 1550 °C) showed approximately the same R-line emission intensity. On the contrary, solid-state prepared sample sintered at 1300 °C showed lower PL intensity. The results indicate one advantageous feature of using nitrates as precursors to prepare luminescent Cr-doped alumina, since it more easily enters the α-phase and forms a better doped sample.

To summarize, the solution-based and solid-state synthesis did not show any significant difference on the photoluminescence properties on the samples after heat treatment at 1550 °C with a hold-up time of 8 h. It was shown that the crystalline phases and possibly the crystal size affect the luminescence properties of the precursor.

4.2.3 Morphology

Figure 25 shows SEM micrographs of Cr-doped alumina prepared with solution-based respectively solid-state method, annealed at 1550 °C, where different morphologies are shown. It seems like the solution-based sample has flake-like morphology while the solid-state method produces more rounded particles. Since the

two samples have similar luminescent yield it may indicate that the morphology is not having a significant impact on the PL.

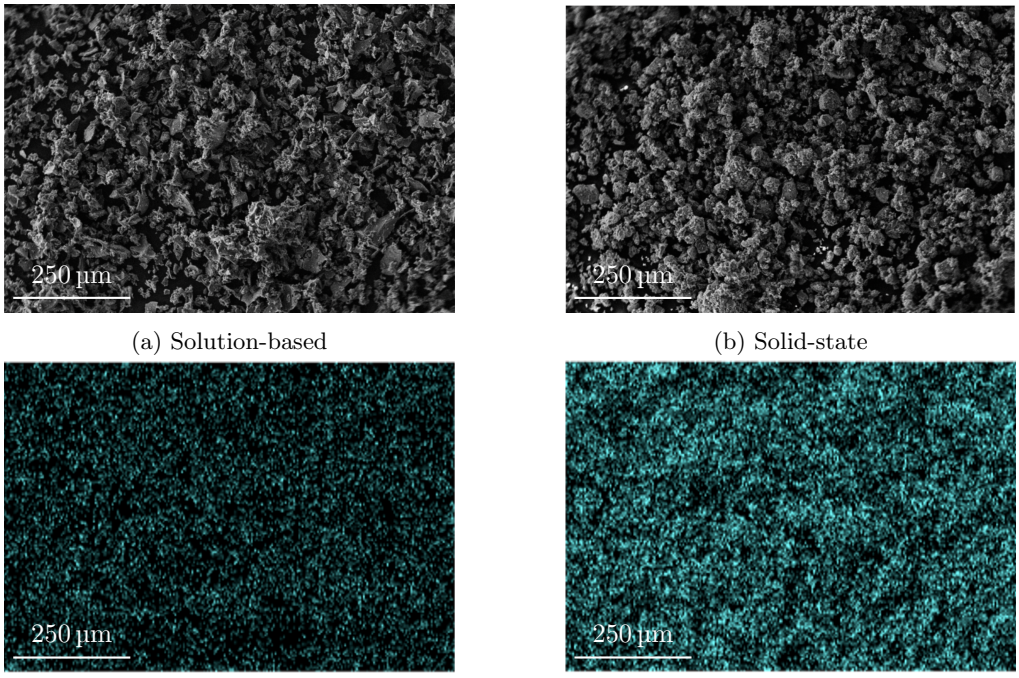

(a) Solution-based

(b) Solid-state

(c) Cr-map of solution-based

(d) Cr-map of solid-state

Figure 25: SEM micrographs of Cr-doped alumina samples from a) the solution-based and b) solid-state synthesis recorded with a secondary electron detector. c) and d) are compositional maps of chromium of the two images above, recorded with a EDS detector.

The powders were also analyzed with EDS to study the dispersion of chromium in the materials. Figure 25d and Figure 25c show the distribution of chromium in the powder samples. The elemental maps of chromium showed poor signal-to-noise ratio, which means that the contribution from the background was considerable. It provides some uncertainties about whether the signal shows homogeneously distributed chromium in the powders or only the background. What can be said is that no pure chromia particles were observed when looking at the Cr-doped powder samples as opposed to the sprayed samples.

Furthermore, the result from the analysis shows somewhat unusual behavior. The EDS spectra of the solution-based powder can be seen in the upper energy spectra in Figure 40 in Appendix D. Two bulky and large, non-characteristic EDS peaks appear in the spectra. This deviation is proposed to be photons emitted from the luminescent material that interferes with the EDS detector. Luminescence in a material can be induced by the electron beam, which is called cathodoluminescene. The interference makes the quantitative and qualitative EDS analysis more difficult, but not to the degree of not detecting pure chromia particles in the sample.

Instead, this phenomenom could be used to investigate the luminescence of materials. There is a study that observed the same phenomenon and showed the possibilities of using SEM-EDS for luminescence characterization of materials [68]. Cathodoluminescence detectors are available as an addition in SEM, but are not as common as EDS detectors. Therefore, this peak broadening was investigated to be used as a qualitative, "quick and dirty" analysis method of luminescence, which enables an easy investigation of luminescent materials with different excitation sources. However, these results of peak broadening could not be reproduced. The second attempt of observing the peak broadening of the same sample gave the spectra shown in the

bottom of Figure 40, which showed an ordinary EDS spectrum without peak broadening. Consequently, the technique needs further studies to be a reliable analysis method for this problem.

4.2.4 Particle size

One of the requirements on the luminescent powder for flame spraying is the precursor particle size. In order to produce coatings with optimal properties using flame spraying pyrolysis, it has been concluded that the precursor particles in the size range of 5-60 µm yield satisfactory products, optimally between 10-45 µm. Therefore, there is interest in investigating the influence that particle size and different grinding techniques have on luminescence. Chromium doped alumina powder (1.5 wt% Cr_2O_3) was ball milled with a stainless steel cup and balls for 5 minutes with a frequency of 20 Hz. The visual change and the particle size difference can be seen in Figure 26, where images of the powders together with corresponding SE-SEM images are shown. The Cr-doped alumina was analyzed with SEM to get a rough estimation of the particle size. By observing these images it can be noted that ball milling with 20 Hz for 5 minutes, considered as high-energy ball milling, significantly reduces the particle size. The image of the non-ball milled sample shows that the powder consists of individual crystalline, faceted particles and also agglomerates of particles. The non-ball milled powder particle size ranges from 20 to 130 µm in diameter whereas the ball-milled sample predominantly consists of particles with diameters of 1-35 µm. It is worth mentioning that these images do not give a statistical and accurate particle size distribution but only an indication of the decrease in particle size.

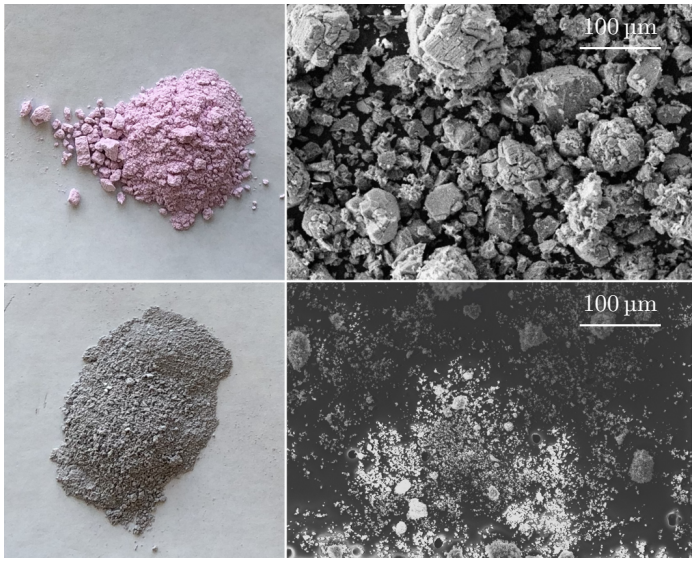

Figure 26: In the top right corner, a Cr-doped alumina powder prior to ball milling with a SE-SEM image of the same powder to the top right. In the bottom left, an image of the Cr-doped powder after ball milling with corresponding SE-SEM image. The ball milling changed the color of the powder from pink to grey.

The color dependency of particle size has been extensively studied for pigments and other powders. The larger surface area of smaller particles increases the reflectance of light, which changes the color of the powder [69]. However, after ball milling the powders, it was observed that the steel balls had gotten a slightly rougher surface. This observation, together with the surprisingly large color change, raised the suspicion of possible powder contamination from the steel balls. Therefore, EDS analysis was performed on the ball-milled powder to see if there was a presence of iron in the powder. The result showed no signs of iron in the powder, concluding that if there is contamination in the sample, it does not exceed the detection limit of the EDS detector. An explanation to why the surfaces of the steel balls appear rougher post ball milling is that some alumina may have reacted with the steel ball under the course of milling, which forms

the rough layer. During high-energy ball milling, steel balls are accelerated to high velocities and smash against the inside wall of the container, which leads to the crushing of particles. As the balls collide with the wall of the container, the large impact and frictional forces create a significant amount of heat, which can be sufficient to activate chemical reactions.

Three XRD measurements were performed on Cr-doped alumina samples before and after they were subjected to various processes; before ball milling, after ball milling, and after ball milling and sintering for 8 h. This was done in order to see how high-energy ball milling affects the crystalline structure of the chromium doped alumina. The results are shown in Figure 27 where pictures of the powders, taken after each treatment, are placed next to the corresponding XRD pattern.

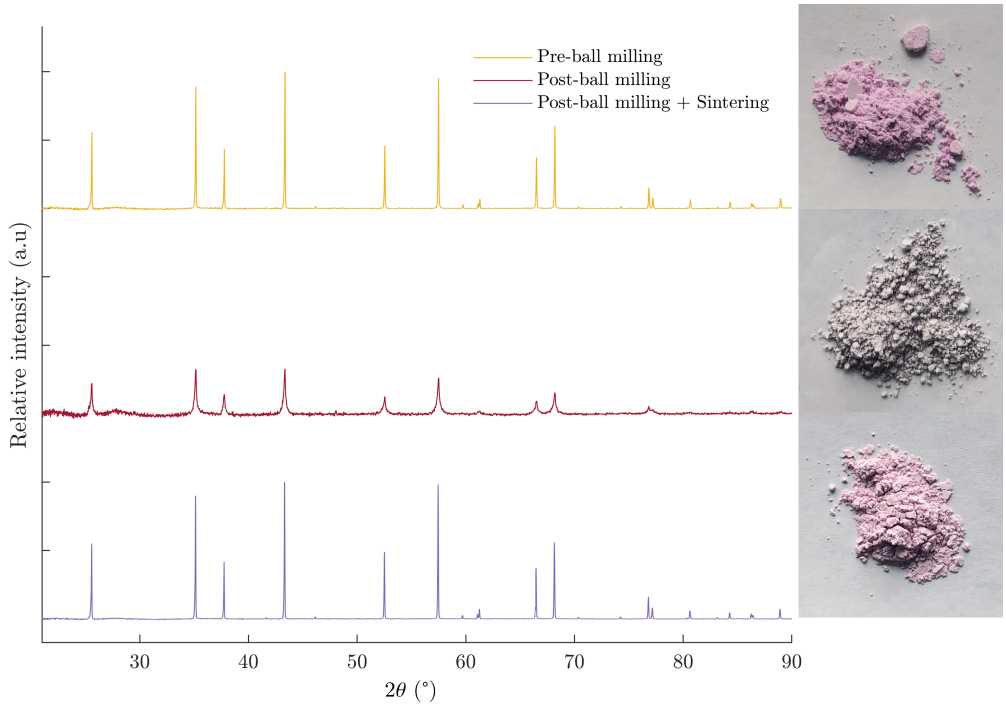

Figure 27: XRD patterns of Cr-doped alumina; before ball milling, after ball milling at 20 Hz for 5 minutes, and after ball milling and re-sintering at 1550 °C for 8 h.

There is a significant difference in the XRD patterns from the sample measured after ball milling compared to "before ball milling" and "after ball milling and the heat treatment". All peaks of the ball-milled sample are smaller and broader. Peak broadening can be an indication of the amorphicity of a specimen, which suggests that the ball milling does in fact change the morphology of the material. After the ball-milled specimen had been sintered once again the α-Al_2O_3 peaks reappeared and, as another confirmation, also regained its characteristic bright pink color for α-Al_2O_3. Very small particles can also be responsible for peak broadening as crystals with a finite number of planes can diffract with slight variations in angles of 2θ due to strain and lattice distortion. The peak intensity predominantly depends on the sample preparation, e.g. the amount of sample placed in the machine for analysis, but can also be affected by the particle size. The reason for the high intensities of the post-sintered sample can be explained by some sort of agglomeration occurring during the heat treatment but needs to be confirmed with further analysis using SEM or any other suitable analysis technique. Imane Ellouzi, I. and Oualid, H. A. came to similar conclusions when they investigated the influence of ball milling on the morphology of TiO_2. The color change and peak broadening were assigned to the decrease of particle size and morphological changes, which supports the conclusions that are drawn from the XRD results [70].

The luminescent properties of the three samples were evaluated with PL measurements and the results are compiled in Figure 28. The luminescence intensity of the doped alumina powder was significantly decreased after being subjected to high-energy ball milling and was only slightly restored after post-ball mill heat treatment. Even though the pre-ball milled sample and the heat-treated sample showed almost identical XRD patterns, their luminescent quality differed significantly. This suggests that the decrease in the luminescence yield is mainly related to the crystallite size of the powder, rather than any phase transition occurring during ball milling. It also concludes that the luminescence cannot be easily restored by heat treatment after ball milling. As earlier mentioned in Section 2.4, several studies have seen that the luminescence yield diminishes with decreasing crystallite size. When studying the SEM images of the pre-milled and the post-ball milled powders in Figure 26 it is shown that the violent grinding of ball milling crushed crystallites to small, down to submicron fractions. The requirements on the particle size for flame spraying still prevents the solid-state synthesized powder from being sprayed without some type of grinding or particle size separation. Due to the loss in luminescence for the high-energy ball mill, further research is highly desired to investigate the possibility of a more gentle ball milling that reduces particle size without crushing crystals.

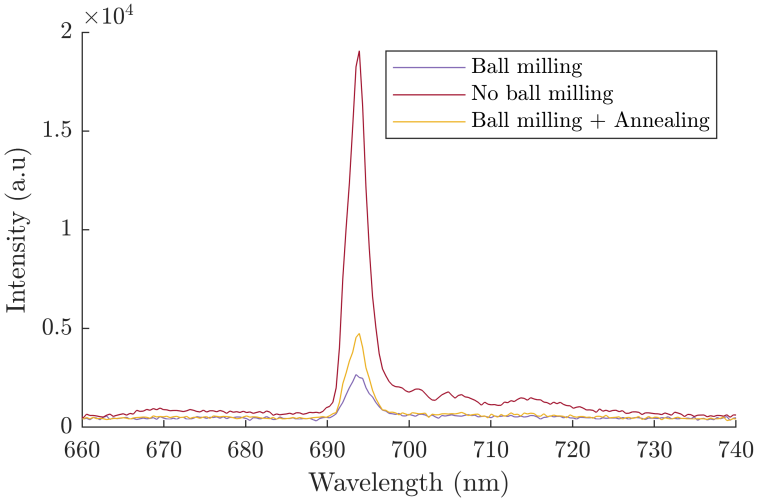

Figure 28: Luminescence measurements on Cr-doped alumina samples, before and after ball milling

4.2.4.1 Sieve analysis

PL measurements evaluated the particle size-dependent PL emission efficiency. The presented results, seen in Figure 29 indicate that the emission intensity from Cr-doped alumina particles in the ranges; < 63µm, 63-75 µm, 75-105 µm and 105-125 µm showed as high emission intensity as the reference sample, which was an un-sieved powder sample. The particles with a size of > 125 µm showed slightly lower emission intensity. However, the intensity is still within a satisfactory range. The observed decrease in intensity may be explained by sample preparation rather than an actual deterioration of the photoluminescence. The retained high PL intensity of smaller particles implies that reducing particles using a mortar and pestle makes the agglomerates fall apart rather than crushing the crystals. The mortar and pestle is, therefore, a more gentle grinding method than high-energy ball milling. Since mortar and pestle is not suitable for grinding larger amounts of powder, further investigations on using low-energy ball milling may be of interest.

4.2.5 Concentration optimization

The doping concentration dependence on photoluminescence was investigated and the results are shown in Figure 30. The plot shows the integrated intensity of the emission spectra between 660 nm to 740 nm upon excitation at 525 nm. It can be seen that the emission intensities are strongly dependent on the dopant concentration. An optimum is found between 0.75 and 1 wt% Cr_2O_3. The few luminescence centers may

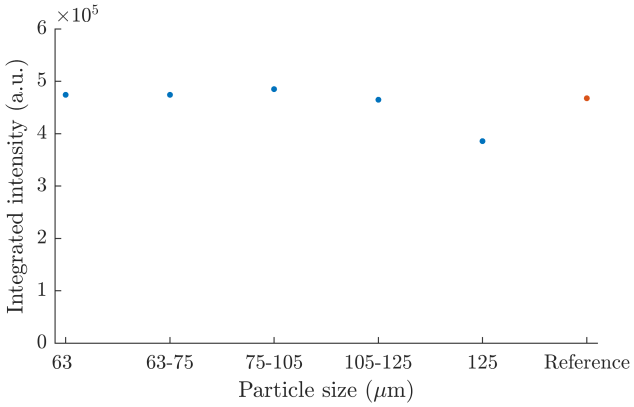

Figure 29: Integrated between 650-750 nm

explain the weak emission intensity at low doping levels; meanwhile at higher doping levels, concentration quenching is the reason for lower emission intensity.

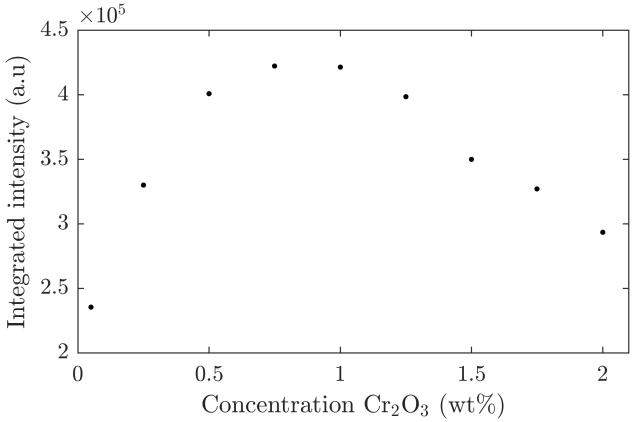

Figure 30: Photoluminescence of Cr-doped alumina over a range of different doping concentration. The intensity of each concentration has been recorded three times and then averaged.

XRF analysis was performed to confirm that the aimed concentrations of Cr_2O_3 in the Cr-doped samples were achieved. The measured concentration in the samples were generally lower than the target concentration. A likely explanation is diffusion of Cr^{3+}-ions into the Al_2O_3 crucible during sintering.

4.2.6 Scale-up

The new precursor has to be flame sprayed in order to see its true performance. XRF analysis confirmed that the scaled-up sample achieved the target concentration 1 wt% Cr_2O_3 in Al_2O_3. XRD patterns of the three different batches can be seen in Figure 41 in Appendix E and it showed that the wanted α-Al_2O_3-phase is obtained and no other phases are observed. The photoluminescence intensity of the bulk batch showed as good luminescence as a small batch, indicating on a successful up-scaling process, see Table 1.

Table 1: Integrated luminescence intensity (650-750 nm) of bulk batch samples and a small batch sample.

Sample	Batch 1	Batch 2	Batch 3	Small batch
Integrated Intensity (a.u)	497000	486000	467000	463000

4.3 Alternative materials

4.3.1 Titanium doped alumina

Two synthesis routes were investigated to produce luminescent titanium doped alumina powder in this study, the solid-state synthesis and the solution-based synthesis. Various parameters were evaluated for both syntheses. Below are the factors for each synthesis that was evaluated.

- Solid-state synthesis
  - Dopant concentration
  - TiO_2 precursor (anatase and rutile)
  - Al_2O_3 precursor (acidic, neutral and basic acitivated)
  - Synthesis temperature (1100 °C and 1550 °C)
  - Pre-sintering treatment (Ball milling or no ball milling)
- Solution-based synthesis
  - Dopant concentration
  - Solvent
  - Synthesis temperature (1100 °C and 1550 °C)

The Ti-doped alumina samples were evaluated with PL spectroscopy. Three excitation sources with 250 nm, 380 nm and 525 nm were used to investigate if the powders exhibited either blue or red emission. Of all the produced samples, none showed any sign of luminescence from the PL measurements. There is no clear reason why the samples did not exhibit any luminescence and one could only speculate about possible explanations. The lack of existing papers on luminescent Ti:alumina powders makes finding the right synthesis parameters more difficult. As stated in Section 2.3.2, the proposed luminescence mechanisms are of complex nature and the varying luminescent behavior could indicate that this material is very sensitive to synthesis parameters and experimental conditions. A few hypotheses on the absence of luminescence are proposed to give some starting points for future studies.

Figure 31 shows XRD measurements of samples prepared using the solution-based synthesis, with titanium concentrations equivalent to 6 wt% TiO_2, that have been annealed at different temperatures. Even though the titanium concentration was considerably higher in comparison to reported luminescent Ti-doped alumina crystals, it was chosen to distinguish an observable change on the XRD pattern when doping the alumina structure. Upon doping, the electron density of certain planes is altered and therefore gives different relative intensities in comparison to structures without extrinsic defects. Differences in ion size can also give rise to peak broadening. From the results, no peak broadening nor shifts in relative intensities were observed. Instead, the material showed to consist of two phases after heat treatment at 1550 °C; Al_2O_5Ti and Al_2O_3. This suggests that Ti^{3+} or Ti^{4+} is not as easily incorporated into the alumina structure as chromium ions, for example. The possibility remains that the alumina structure has been doped in insufficiently large amounts for observable changes on the XRD pattern. However, the absence of luminescence properties could be explained by the fact that no doping has occurred. In Section 2.3.2, the Czochralski method is briefed where precursor materials are melted at very high temperatures. The melt improves the homogeneity and the rapid

cooling prevents segregation into the Al_2O_5Ti and Al_2O_3 phases. Heat treatments to higher temperatures than 1550 °C is a proposition to increase the diffusion of titanium ions that could facilitate doping.

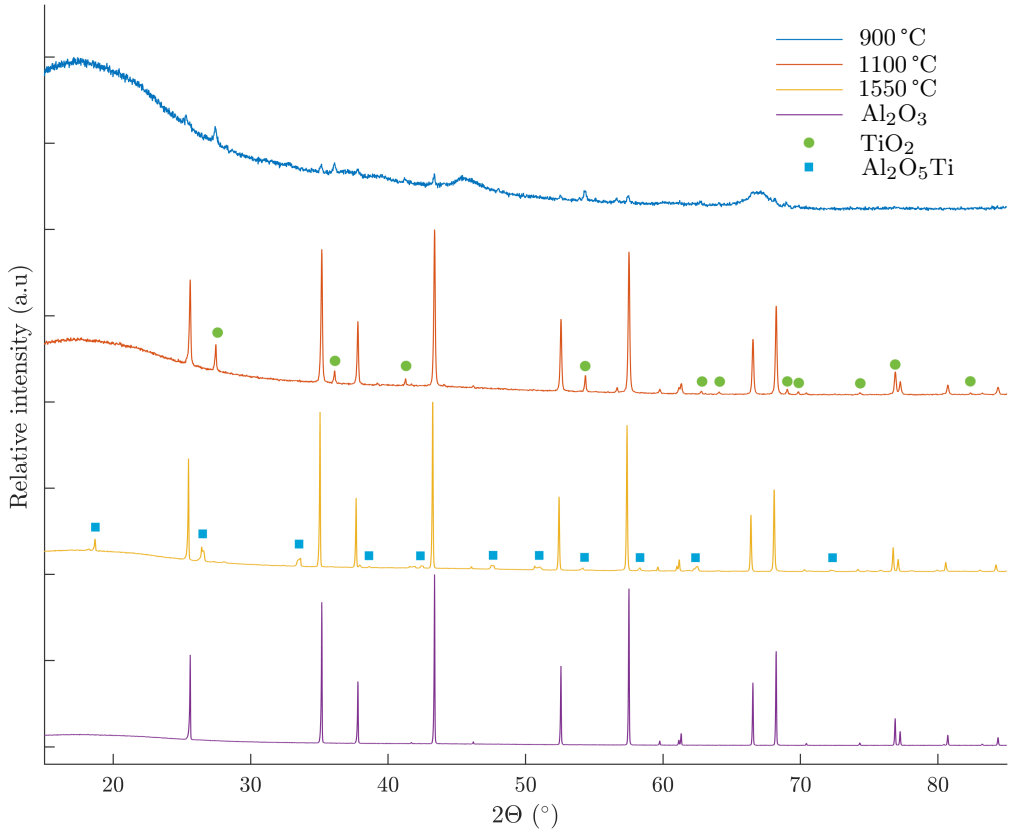

Figure 31: XRD of titanium alumina prepared with the solution synthesis at different annealing temperatures compared with pure α-alumina.

One of the advantages of the solution-based synthesis is that Ti^{4+} and Al^{3+} are dissolved and therefore completely mixed in the solution. After solvent evaporation, the good mix of titanium-aluminum-oxides facilitates diffusion of Ti^{4+} into the alumina structure later during sintering. However, the presence of rutile TiO_2 was observed at 900 °C and 1100 °C. This suggests that the titanium oxide has formed clusters and not fully been mixed with the alumina. In the solution-based synthesis, titanium dioxide and alumina are co-precipitated by the addition of water. During the screening, it was observed that the precipitation rate of titanium(IV) isopropoxide was higher than for aluminum(III) isopropoxide. As a consequence, the desired aluminum-titanium-oxide complexes were not formed as hoped and therefore make the solution-based method less advantageous than expected.

Most papers have studied the luminescence of single-crystal Ti-doped alumina instead of polycrystalline Ti-doped alumina. Polycrystalline materials significantly have a higher density of defects in comparison to monocrystalline materials. Defects, such as F-centers and aluminum vacancies (V_{Al}^{3+}) are optically active. If the defects absorb in the same region as the other mechanisms in the material emit light, the luminescence is suppressed. This phenomenon is called parasitic absorption [36], which is a possible explanation for the lack of luminescence. Parasitic absorption, or defects in crystals more generally, have shown to diminished upon heat treatment in a reducing environment. Due to the lack of equipment, the influence of high-temperature heat treatment in reducing environment on the luminescence has not been investigated in this study.

There might also be a risk that the energy levels of the three light sources (525, 380 and 250 nm) that

were used did not overlap with the absorption spectra of the produced samples. There are publications where photoluminescence measurements were performed with excitation sources with higher energy, such as 175 and 210 nm [32]. However, the ambiguity on what parameters inhibit the luminescence makes further research on Ti-doped alumina difficult to motivate. Instead, the work continues with Ce:YAG as a possible alternative luminescent material for PBI at ESS.

4.3.2 Cerium doped YAG

To examine whether the yttrium aluminum garnet was successfully synthesized, the crystallographic structure of the material was analyzed with XRD and the result can be seen in Figure 32. The XRD pattern exhibited sharp distinguishable diffraction peaks, which indicates high crystallinity. The diffraction peaks can be indexed to a YAG phase and a $YAlO_3$-phase, also known as Yttrium-Aluminum-Perovskite (YAP) structure. After a Rietveld refinement, the fraction of $YAlO_3$-phase was determined to be 1.5 wt%. The presence of the $YAlO_3$-phase may potentially be due to incorrect stoichiometry being obtained while weighing up the starting materials. If the overall stochiometry is correct, the YAP phase could form due to inhomogeneity in the mixture. A local excess of yttrium oxide leads to the formation of the YAP phase, but in turn would also form an Al_2O_3 phase maintain the stoichiometric equilibrium. Based on the XRD patterns, alumina is not observed but could be present below the detectable limit. As mentioned in Section 3.3.2, the crucibles used for the heat treament were made of alumina, which inevitably will interact with the Ce:YAG. Diffusion into or reaction with the alumina crucible can disturb the stoichometry of the powder that prevents the formation of a 100 % YAG-phase.

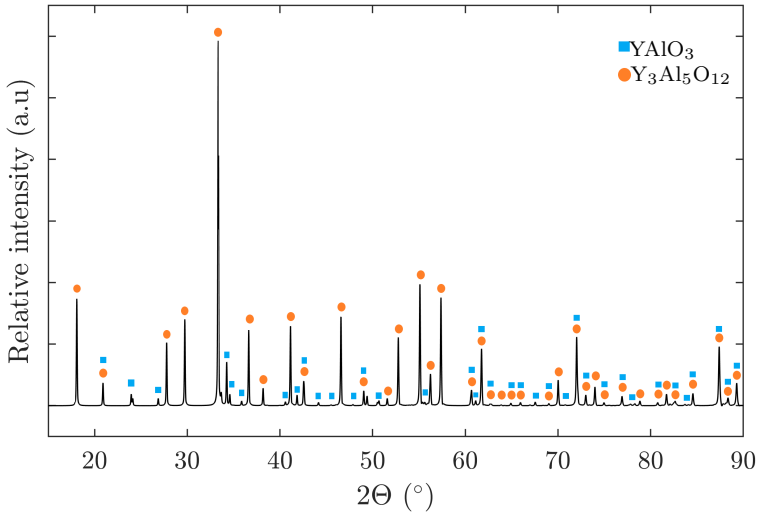

Figure 32: Diffractogram of YAG, synthesized using the solution-based synthesis and sintered at 1550 °C.

Photoluminescence spectroscopy was used to evaluate the luminescent properties of the synthesized Ce-doped YAG. During excitation with a 380 nm UV source of the Ce-doped YAG a broad emission band was observed from 500 to 650 nm, which can be seen in the emission spectrum in Figure 33.

The photoluminescence intensity-to-noise ratio were relatively low, which can be explained by the fact that the optimum of the Ce:YAG absorption band is around 460 nm and that the excitation was a 380 nm UV source. However, peak broadening of the UV source extends in the blue spectra, which enables excitation of the Ce-doped YAG. By changing the UV source to a more appropriate source, the signal-to-noise ratio will be enhanced. The results from the cerium concentration dependence on the photoluminescence intensity can be seen in Figure 34. The cerium concentration that yielded the brightest luminescence was 1.6 mol% Ce^{3+}-ion relative to YAG. The luminesence intensity of the 1.6 mol% Ce:YAG slightly deviates from the rest of the measurements. This motivates further measurements with data points close to 1.6 mol% in order to obtain a

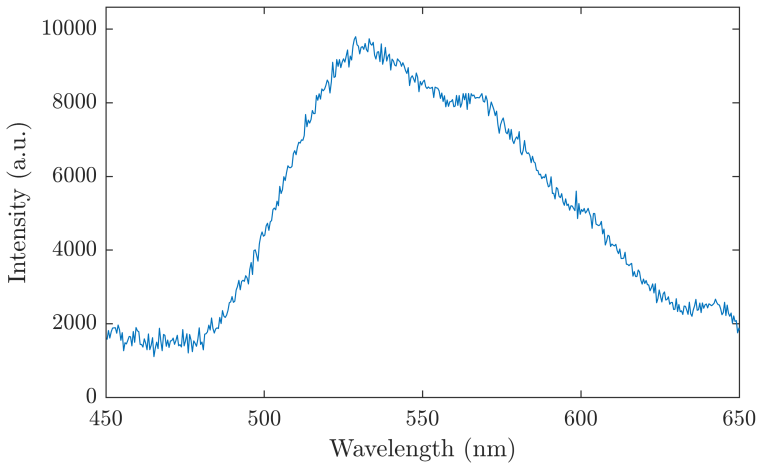

Figure 33: Photoluminescence emission spectra of 1 wt% Ce:YAG.

smooth curve. As mentioned in Section 2.3.3, studies have shown that concentration quenching of Ce-doped YAG with doping levels above 1 mol% occurs at significantly lower temperatures than concentration levels below 1 mol%. Concentration quenching starts, according to the study, at 400K. As the target wheel is expected to rise to temperatures above 400K during operation, this quenching effect needs to be measured and taken into account before the material is chosen as an alternative luminescent material for PBI imaging.

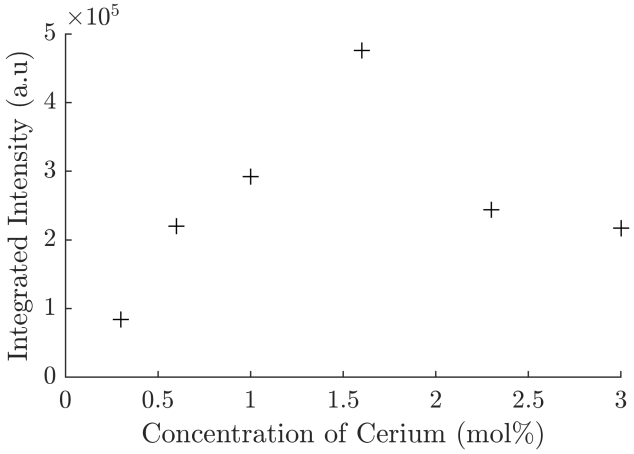

Figure 34: Photoluminescence measurements of Ce:YAG with different Cerium concentrations; 0.3, 0.6, 1, 1.6, 2.3, 3 mol%, excited with a 350 UV excitation source.

It is worth mentioning that studies show that there is an optimum particle size of Ce-doped YAG when it comes to forming the highest photoluminescence intensity. In turn, the particle size can be controlled by the sintering temperature [43]. This is something that needs to be further investigated to obtain a better luminescent material. Additionally, improvements on the synthesis method of Ce-doped YAG are essential before a potential up-scaling since the prepared sample contain not only the single YAG phase.

5 Conclusion

A selection of sprayed samples, produced by thermal spraying at University West (Trollhättan), were investigated to study how the luminescent properties are affected by coating thickness and spraying technique. XRD patterns showed that the crystalline structure of the samples was predominantly in the α-alumina but with existing fractions of the η-alumina to various degrees. The PL measurements revealed that 100 µm yielded the strongest R-line emission intensity and the lowest emission intensities came from the extremities of 50 µm and 300 µm. The inferior performance of 50 µm was expected as the theory suggests that decreasing thickness has weaker luminescence. On the other hand, an explanation to the lower luminescence of the 300 µm was undiscovered.

The comparison of the two spraying techniques showed that plasma spraying produces brighter coatings than flame spraying with equal thickness. The $\alpha \rightarrow \eta$-alumina transition was shown to be suppressed by plasma spraying relative to the flame spraying, which concurs with the PL measurements since α-alumina is known for its superior luminescent properties. SEM-EDS images of the sprayed samples showed particles of pure Cr_2O_3, which suggests incomplete incorporation of the Cr^{3+} ions. This suggests that the in-time Cr-doping during flame spraying might make accurate doping levels difficult to achieve.

To produce a Cr-doped alumina precursor for flame spraying, two synthesis routes were extensively investigated and evaluated based on the luminescent properties of the powders. Both syntheses produced a bright pink powder that exhibited strong characteristic ruby-line emission upon green laser excitation. The solid-state method turned the precursor from light green → white → pink in color with increasing sintering temperature, which corresponds to crystallization into the η-Al_2O_3 and incorporation of the Cr^{3+} followed by the phase transition to α-Al_2O_3, respectively. Solution-based synthesized powders showed a similar morphological evolution, but the crystallization and the $\eta \rightarrow \alpha$ phase transition occurred at lower temperatures. Consequently, the solution-based synthesis produced powders with superior luminescent properties compared to the solid-state method after heat treatment at 1100 °C and 1300 °C. However, increasing the sintering temperature to 1550 °C produced equally bright luminescent powders. The morphology of the powders was distinct but did not have a significant impact on the luminescence. The doping concentration of Cr^{3+}-ions was optimized with PL measurements on solid-state synthesized powders. 1 wt% of Cr_2O_3 gave the brightest powder but the luminescence was rather insensitive to variations between 0.5 - 1.25 wt% of Cr_2O_3.

The impact of grinding techniques on luminescence was investigated to prepare precursor materials for flame spraying. High-energy ball milling turned the pink powder grey, which was explained by the crushing of crystallites into submicron fractions. Consequently, the luminescent intensity dropped significantly. Even though the powder regained its pink color after heat treatment at 1550 °C, the luminescence was only slightly recovered. As an alternative method, grinding with mortar and pestle reduced the particles to an appropriate size by breaking up agglomerates without damaging the crystals, which led to the material retaining its luminescent properties.

The moderately long luminescence lifetime of Cr-doped alumina motivated the research on alternative luminescent materials for PBI. The attempt to synthesize titanium doped alumina was made via two synthesis routes: solution-based and solid-state synthesis. PL measurements performed on the Ti:alumina samples showed no sign of luminescence. Due to the many possible explanations for the lack of luminescence, the study on Ti-doped alumina was not further pursued. With greater success, a yellow powder made of Ce:YAG was synthesized using the solution-based synthesis that exhibited a characteristic green-yellow emission upon 460 nm blue excitation. A doping concentration screening revealed that 1.6 mol% Ce:YAG yielded the brightest luminescence. Small fractions of the YAP phase present could be explained by interaction with the crucible during sintering.

To conclude, findings from the analysis of spray coated samples lay the groundwork for the proposed precursor preparation in this study. After a thoroughly investigation of the nature of the new precursor to optimize its luminescent properties, a pink, Cr-doped alumina precursor with excellent luminescent properties has been successfully produced. Furthermore, a luminescent Ce-doped YAG powder with favourably short

luminescence lifetime has been successfully produced, which adds to the list of alternative materials for proton beam imaging.

5.1 Future work

More sprayed samples with varying thickness are required to get a better understanding how thickness impacts the crystal structure. The data will help to further develop the thickness normalization model that can enable comparison of not only samples with different thickness, but also comparing sprayed samples with powders.

The Cr-doped alumina powdered precursor has been successfully synthesized and prepared for flame spray pyrolysis. By flame-spraying the sample and producing a coating, a fair comparison between the Brodmann powder sprayed samples and the new precursor can be done. The Ce-doped YAG shows promising results but requires optimization on the synthesis route to obtain 100 % of the YAG phase. Measuring the luminescence lifetime of Ce-doped YAG and Cr-doped alumina can confirm what has been stated in the literature. Photon yield measurements on Cr-doped alumina and Ce-doped YAG will reveal what material exhibits the brightest luminescence. The material that exhibits the best luminescent properties can be further evaluated on the radiation resistance, oxidation resistance and luminescent temperature dependence. If a material can be developed to meet all the requirements for luminescent materials for PBI, the safety of the Target wheel can be assured - one of the most important and expensive equipment at ESS.

A XRD pattern

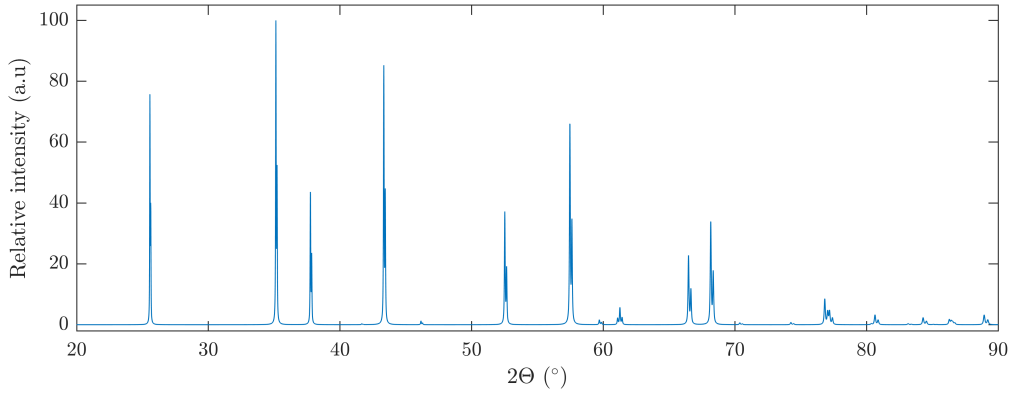

Figure 35: XRD pattern of α-Al_2O_2

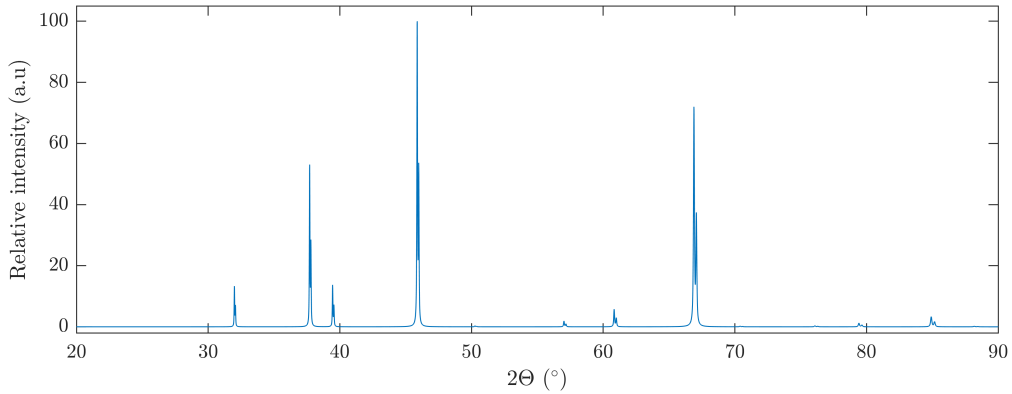

Figure 36: XRD pattern of η-Al_2O_2

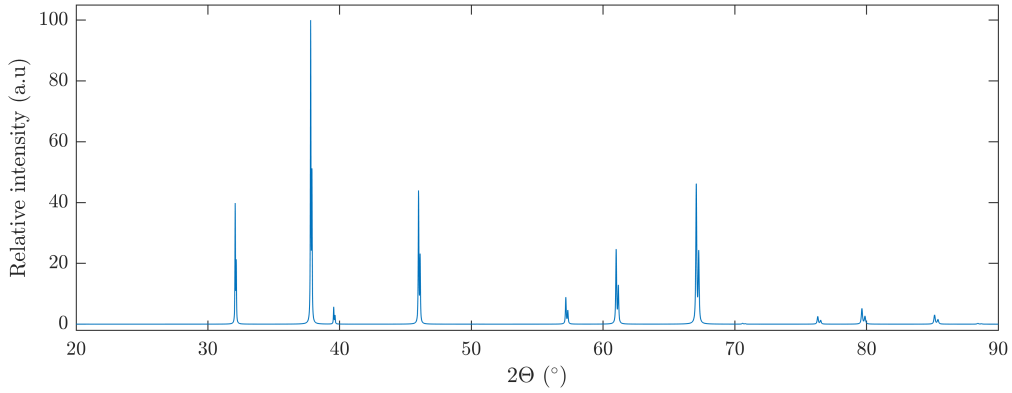

Figure 37: XRD pattern of γ-Al_2O_2

B Brunauer–Emmett–Teller and Langmuir

Brunauer–Emmett–Teller (BET) and Langmuir are two theories from which the specific surface area and porosity of a material can be determined. The methods are based on the absorption of gas molecules onto the surface of the solid material. By dosing a non-corrosive gas, ordinary nitrogen, in a series of different pressures, the solid surface will completely be covered with layers of the gas molecules, so-called adsorbates. The amount of adsorbate depends on the relative vapor pressure, $\frac{p}{p_0}$, of nitrogen at 77.4 K and by measure the amount of adsorbate at different pressures, the specific surface area and porosity of the material can be determined of the material. The Langmuir theory model assumes that the surface is covered with only a mono-layer of the adsorbate; however, this does not reflect the truth. BET equation takes into account the multi-layers of adsorbates and therefore models the surface area and porosity more precisely. Materials that are commonly analyzed with the BET method are, for example, ceramics, catalysts and pharmaceuticals [71].

In this thesis, the surface area and porosity of the samples were analyzed by a Micromeritics-Gemini IIV. The relative vapor pressure was increased from 0.055 to 0.25 and then the software called Optional Gemini Windows Software determined both the BET and Langmuir surface area by measuring the number of adsorbates.

B.1 Results BET

BET measurements were performed on Cr-doped alumina to investigate if Cr_2O_3 potentially influence the surface area of the powder. A change in surface area can be an indication of agglomeration of particles, which may affect the incorporation of chromium ions into the alumina structure upon sintering. This is an important aspect of the solid-state synthesis of Cr-doped alumina. Four samples were analyzed with BET, and the results are compiled in Table 2 below. The purchased alumina powder exhibits a high surface area of 117.3 m^2/g, but after thermal treatment at 1550 °C for 8 h the surface area drops to 0.8 m^2/g. The chromium doped alumina and the unsintered alumina show similar surface areas of 0.8 m^2/g and 0.8 m^2/g, respectively. The chromium doped alumina sample that has been sintered at 1100 °C has a surface area of 7.3 m^2/g.

Table 2: The BET specific surface area

Sample	Sintering temperature	BET surface area (m^2/g)	Langmuir surface area (m^2/g)
Pure alumina	Not sintered	117.3	173.8
Pure alumina	1500 °C	0.820	
Cr-doped alumina (1.5 wt%)	1100 °C	7.3	10.6
Cr-doped alumina (1.5 wt%)	1550 °C	0.9	1.3

From the BET measurements, it can be concluded that the sintering affects the surface area drastically. The largest difference seen from the results is between the unsintered sample and the sintered samples. The surface area drops from 117.3 m^2/g to 0.8 m^2/g of pure alumina upon sintering to 1550 °C and the explanation for the difference point towards crystallization. It is known that when a material crystallizes, the atoms rearrange in a densely packed structure. The high surface area of the unsintered powder indicates that the purchased powder is amorphous and porous. The surface area of the powder that has been sintered at 1100 °C sits appropriately between the unsintered and the 1550 °C sintered sample. The most interesting observation from the BET measurements is that the surface area of sintered pure alumina and chromium doped alumina are almost identical, showing that the chromium oxide does not contribute to agglomeration of the powder. If agglomeration would occur when mixing alumina and chromia powders, it could obstruct the diffusion of dopants when the material is being sintered. This could possibly favor the solution synthesis even further, which minimizes the required diffusion length. Since it has been reported in the literature that

large crystallite size increases the luminescent intensity of powders and that a large crystal size leads to a small surface area, BET measurements are also proposed as a quick and rough comparative analysis method to foresee the luminescent quality of a material.

C Thickness normalization model of PL measurements

A model has been developed and evaluated for thickness normalization in this study. The apparent PL intensity can be normalized by taking absorption and reflectance into consideration to derive a material-characteristic photon yield. Figure 38 is a simplification of the PL measurements. The material is excited along the z-axis with a pencil beam excitation source. A detector is placed parallel to the excitation source and collects emitted light from the material. The assumption in this derivation is that the collection of light is from a small solid angle, which is assumed to be constant for all point sources in the material. The thickness of the coating is $z_d = z_1 - z_0$.

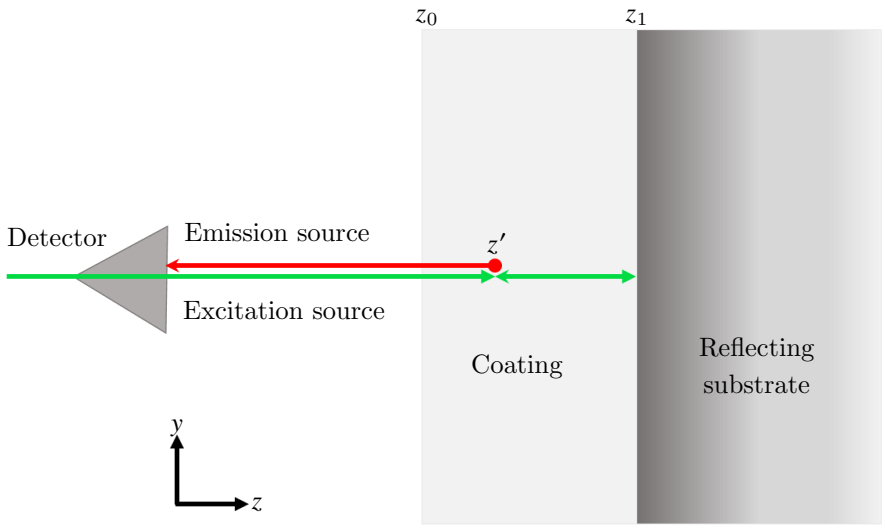

Figure 38: A schematic image of photoluminescence of a sample attached to a reflecting surface.

The excitation source has the characteristic absorption coefficient α_0 and the reflectance R_0. The coating absorbs the emitted light with the absorption coefficient α_1 and reflects on the substrate with the reflectance R_1.

A point source, marked as the red dot, is then emitting light which is scaled by the photon density of the excitation light at that depth. The emission intensity from the point source located at a depth z' can be explained by Equation 4:

$$dI = \frac{I_0}{2}\left(e^{-\alpha_0 z'} + R_0 e^{-\alpha_0(2z_d - z')}\right)\left(e^{-\alpha_1 z'} + R_1 e^{-\alpha_1(2z_d - z')}\right) \tag{4}$$

where the first factor expresses the photon density of the excitation source, which is proportional to the incident power and the second factor represents the emitted light.

$$I = \int_0^{z_d} \frac{I_0}{2}\left(e^{-\alpha_0 z'} + R_0 e^{-\alpha_0(2z_d - z')}\right)\left(e^{-\alpha_1 z'} + R_1 e^{-\alpha_1(2z_d - z')}\right) dz' \tag{5}$$

Integrating dI between 0 to z_d summarizes the emitted light over all point sources along the z-axis in the material, which is expressed as Equation 6.

$$I = \frac{I_0}{2}\left[\frac{1 - e^{-(\alpha_0+\alpha_1)z_d}}{\alpha_0 + \alpha_1} + R_0 e^{-2\alpha_0 z_d}\frac{1 - e^{-(\alpha_1-\alpha_0)z_d}}{\alpha_1 - \alpha_0} + R_1 e^{-2\alpha_0 z_d}\frac{1 - e^{-(\alpha_0-\alpha_1)z_d}}{\alpha_0 - \alpha_1} + R_0 R_1 e^{-2(\alpha_0+\alpha_1)z_d}\frac{1 - e^{-(\alpha_0+\alpha_1)z_d}}{\alpha_0 + \alpha_1}\right] \tag{6}$$

The material characteristic absorption length for red emission light has been experimentally determined to be 185 µm in Cr-doped alumina. The absorption length for green light and the reflectances R_0 and R_1 were fitted to the data, seen in Figure 39, to 250 µm, 0.9 and 0.91 respectively. The model has been developed and constants have been calculated by Thomas, C. at ESS [67].

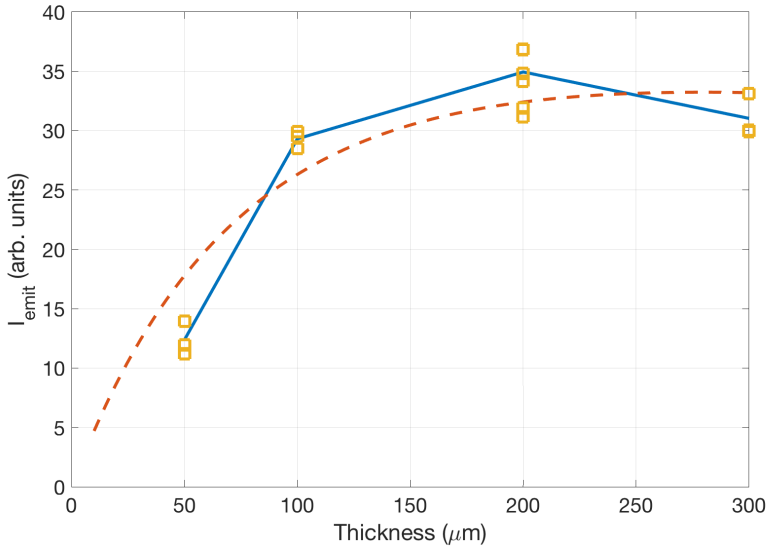

Figure 39: Model fitted to the luminescence intensities of sprayed samples with varying coating thickness. The image is adapted 2021-05-27 from Thomas, C., 2021 [67].

In Equation 6, I is the measured intensity and by solving the equation for I_0, the material characteristic PL yield is obtained and sprayed samples with different thicknesses can be compared.

D Energy dispersive X-ray spectroscopy

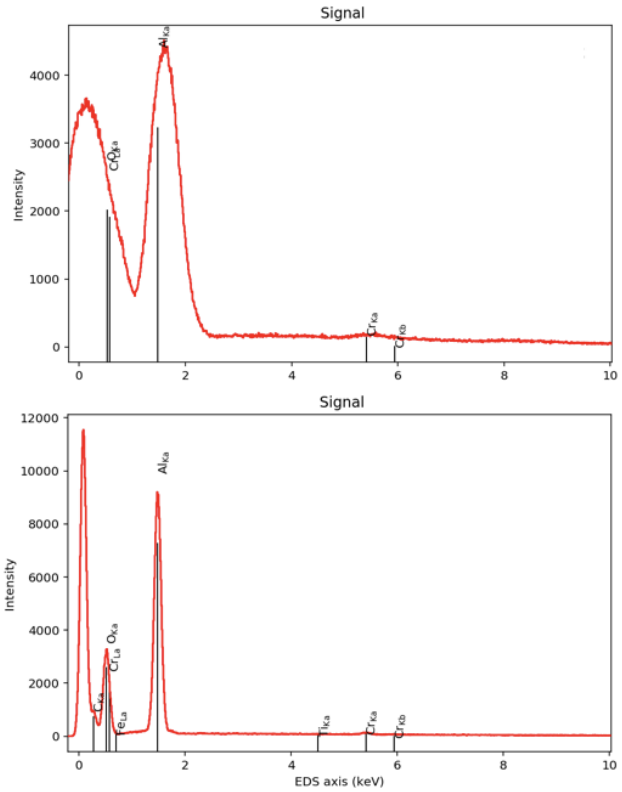

Figure 40: EDS spectra of Cr-doped alumina powder, measured at two different times.

E XRD pattern of sample prepared for flame spraying

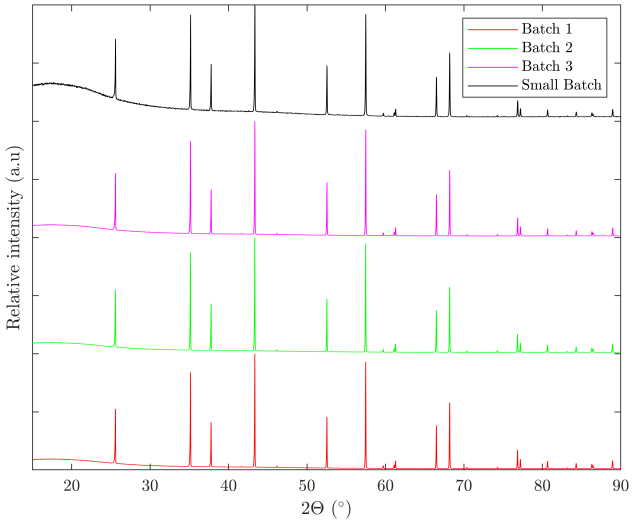

Figure 41: XRD patterns of three Cr-doped bulk batches compared with a small size batch och the same material.

References

[1] E. Adli et al. "The ESS Target Proton Beam Imaging System as in-Kind Contribution" (2017), p. 4.

[2] M. Lindroos et al. "Status of the ESS Accelerator Construction Project". *Proceedings of the 6th Int. Particle Accelerator Conf.* (2015). DOI: 10.18429/JACOW-IPAC2015-THPF080. (Visited on 02/12/2021).

[3] *European Spallation Source*. (2021). URL: https://europeanspallationsource.se/technology (visited on 02/12/2021).

[4] F. Sordo. "Proton Beam Window & Tunning beam dump" (2018), p. 33.

[5] B. P. Kafle. "Molecular luminescence spectroscopy". In: *Chemical Analysis and Material Characterization by Spectrophotometry*. Elsevier, 2020, pp. 269–296. DOI: 10.1016/B978-0-12-814866-2.00009-9. (Visited on 02/21/2021).

[6] H. Gjersdal. "Plan for the protection of Target Imaging Systems Mirrors against Corrosive Environment" (2017), p. 6.

[7] J. Tian et al. "Temperature and Optimize Design of Beam Window in the Accelerator". *New York* (2011).

[8] C. Thomas et al. "Preliminary Measurement on Potential Luminescent Coating Material for the ESS Target Imaging Systems" (2016), p. 4. DOI: 10.18429/JACoW-IBIC2016-TUPG82.

[9] O. Amsellem et al. "A composite approach to Al_2O_3 based plasma-sprayed coatings" (2006), p. 6.

[10] G. Blasse and B. C. Grabmaier. *Luminescent Materials*. Berlin, Heidelberg: Springer Berlin Heidelberg, 1994. DOI: 10.1007/978-3-642-79017-1. (Visited on 02/12/2021).

[11] G. Salek et al. "Optical properties versus temperature of Cr-doped γ- and α-Al_2O_3 : Irreversible thermal sensors application". *Journal of Luminescence* (2016), pp. 189–196. DOI: 10.1016/j.jlumin.2016.07.004. (Visited on 04/11/2021).

[12] M. Ghamnia, C. Jardin, and M. Bouslama. "Luminescent centres F and F+ in alfa-alumina detected by cathodoluminescence technique". *Journal of Electron Spectroscopy and Related Phenomena* 133.1-3 (2003), pp. 55–63. DOI: 10.1016/j.elspec.2003.08.003. (Visited on 03/31/2021).

[13] A. Kitai. *Luminescent materials and applications*. Wiley series in materials for electronic and optoelectronic applications. England: John Wiley, 2008. DOI: 10.1002/9781119529538.

[14] Y. Tanabe and S. Sugano. "On the Absorption Spectra of Complex Ions. I". *Journal of the Physical Society of Japan* (1954), pp. 753–766. DOI: 10.1143/JPSJ.9.753. (Visited on 04/21/2021).

[15] A. Edgar. "Luminescent Materials". In: *Springer Handbook of Electronic and Photonic Materials*. Cham: Springer International Publishing, 2017. DOI: 10.1007/978-3-319-48933-9_38. (Visited on 02/05/2021).

[16] *Alumina*. 2020, p. 1.

[17] T. Shirai et al. "Structural Properties and Surface Characteristics on Aluminum Oxide Powders" (2009), p. 9.

[18] V. Tsirelson et al. "Ruby structure peculiarities derived from X-ray diffraction data localization of chromium atoms and electron deformation density". *Physica status solidi (a)* 87.2 (1985), pp. 425–433. DOI: https://doi.org/10.1002/pssa.2210870204.

[19] Q. Liu et al. "The thermoluminescence and optically stimulated luminescence properties of Cr-doped alpha alumina transparent ceramics". *Journal of Alloys and Compounds* 579 (2013), pp. 259–262. DOI: 10.1016/j.jallcom.2013.06.070.

[20] J. Hecht. "Short history of laser development". *Optical Engineering* 49.9 (2010). DOI: 10.1117/1.3483597. (Visited on 04/09/2021).

[21] D. Liu. "Effects of Cr content and morphology on the luminescence properties of the Cr-doped alpha-Al2O3 powders". *Ceramics International* 39.5 (2013), pp. 4765–4769. DOI: 10.1016/j.ceramint.2012.11.063. (Visited on 04/22/2021).

[22] D. Chandler et al. "Ruby Crystal for Demonstrating Time- and Frequency-Domain Methods of Fluorescence Lifetime Measurements". *Journal of Fluorescence* 16.6 (2006), pp. 793–807. DOI: 10.1007/s10895-006-0123-7. (Visited on 04/21/2021).

[23] E. Sorokin. "Solid-State Materials for Few-Cycle Pulse Generation and Amplification". In: *Few-Cycle Laser Pulse Generation and Its Applications*. Vol. 95. Berlin, Heidelberg: Springer Berlin Heidelberg, 2004, pp. 3–73. DOI: 10.1007/978-3-540-39849-3_1. (Visited on 04/21/2021).

[24] Y.L. Zhu et al. "Effects of Cr3+ concentration on the crystallinity and optical properties of Cr-doped Al2O3 powders by solid-state reaction method". *IOP Conference Series: Materials Science and Engineering* 382 (2018), p. 022037. DOI: 10.1088/1757-899X/382/2/022037. (Visited on 04/22/2021).

[25] M. Xiaoyun et al. "Preparation and luminescent properties of Cr3+:Al2O3 nano-powders by low-temperature combustion synthesis". *Advanced Powder Technology* 20 (2009), pp. 164–168. DOI: 10.1016/j.apt.2008.06.003.

[26] H. Scheel. "Historical aspects of crystal growth technology". *Journal of Crystal Growth* 211.1-4 (2000), pp. 1–12. DOI: 10.1016/S0022-0248(99)00780-0. (Visited on 04/24/2021).

[27] "Structural and photoluminescent properties of Al2O3: Cr3+ nanoparticles via solution combustion synthesis method". *Advanced Powder Technology* 25 (2014), pp. 767–772. DOI: 10.1016/j.apt.2013.11.009.

[28] R. Ianoș et al. "Combustion synthesis of pink chromium-doped alumina with excellent near-infrared reflective properties". *Ceramics International* 43.2 (2017), pp. 2568–2572. DOI: 10.1016/j.ceramint.2016.11.061. (Visited on 04/24/2021).

[29] N. Lyamkina et al. "Ultrafine Cr-Doped Al2O3 Prepared by Detonation Synthesis". *Inorganic Materials* 41.8 (2005), pp. 830–835. DOI: 10.1007/s10789-005-0221-y. (Visited on 04/26/2021).

[30] P. F. Moulton. "Spectroscopic and laser characteristics of Ti:Al2O3". *J. Opt. Soc. Am. B* 3.1 (1986), pp. 125–133. DOI: 10.1364/JOSAB.3.000125.

[31] M. Fermann, A. Galvanauskas, and G. Sucha. *Ultrafast lasers: technology and applications*. Vol. 80. CRC Press, 2002.

[32] V.B. Mikhailik et al. "Studies of concentration dependences in the luminescence of Ti-doped Al2O3". *Journal of Applied Physics* 109 (2011), pp. 053116–. DOI: 10.1063/1.3552943.

[33] V.B. Mikhailik et al. "Luminescence studies of Ti-doped Al2O3 using vacuum ultraviolet synchrotron radiation". *Applied Physics Letters* 86 (2005), pp. 101909–101909. DOI: 10.1063/1.1880451.

[34] R. Powell et al. "Thermal effects on the optical spectra of Al2O3:Ti3+". *The Journal of Chemical Physics* 84.2 (1986), pp. 662–665. DOI: 10.1063/1.450561.

[35] R. Withnall. "SPECTROSCOPY — Raman Spectroscopy". In: *Encyclopedia of Modern Optics*. Elsevier, 2005, pp. 119–134. DOI: 10.1016/B0-12-369395-0/00960-X. (Visited on 03/31/2021).

[36] M. Yamaga et al. "Optical and electron spin resonance spectroscopy of Ti3+ and Ti4+ in Al2O3". *Journal of Applied Physics* 75.2 (1994), pp. 1111–1117. DOI: 10.1063/1.356494.

[37] "Crystal Growth, Bulk: Methods". In: *Encyclopedia of Condensed Matter Physics*. Ed. by B. Franco, L. Gerald, and W. Peter. Oxford: Elsevier, 2005, pp. 262–274. DOI: 10.1016/B0-12-369401-9/00416-2.

[38] Z. Guiping, D. Qiang, and B. Weitao. "Luminescent properties of Ti3+-doped γ-Al2O3 powder". *Journal of Physics D: Applied Physics* 46 (2013), p. 305301. DOI: 10.1088/0022-3727/46/30/305301.

[39] G. Molnár et al. "Photoluminescence and thermoluminescence of titanium ions in sapphire crystals". *Radiation Measurements* 33.5 (2001), pp. 663–667. DOI: 10.1016/S1350-4487(01)00080-4.

[40] Y. Hidehiro, H. Keijiro, and Y. Takahisa. "Densification Behavior of Ti-Doped Polycrystalline Alumina in a Nitrogen-Hydrogen Atmosphere". *MATERIALS TRANSACTIONS* 50.5 (2009), pp. 1032–1036. DOI: 10.2320/matertrans.MC200829.

[41] T. Daimon et al. "Study of Blue Photoluminescence in Titanium Doped Al2O3 Single-Crystals". *Iop Conference Series: Materials Science and Engineering* 18 (2011). DOI: 10.1088/1757-899X/18/10/102012.

[42] H. Burton et al. "Temperature dependence of Ti:Sapphire fluorescence spectra for the design of cryogenic cooled Ti:Sapphire CPA laser". *Opt. Express* 25.6 (2017), pp. 6954–6962. DOI: 10.1364/OE.25.006954.

[43] X.H. Yan et al. "Preparation of YAG:Ce3+ phosphor by sol-gel low temperature combustion method and its luminescent properties". *Transactions of Nonferrous Metals Society of China* 18.3 (2008), pp. 648–653. DOI: 10.1016/S1003-6326(08)60113-2.

[44] V.M. Bachmann, C. Ronda, and Andries Meijerink. "Temperature Quenching of Yellow Ce3+ Luminescence in YAG:Ce". *Chemistry of Materials* 21 (2009). DOI: 10.1021/cm8030768.

[45] K. Walter. *Solid-State Laser Engineering*. Springer, 2006. DOI: 10.1007/0-387-29338-8.

[46] U. Jumpei and T. Setsuhisa. "(INVITED) Review of luminescent properties of Ce3+-doped garnet phosphors: New insight into the effect of crystal and electronic structure". *Optical Materials: X* 1 (2019), p. 100018. DOI: 10.1016/j.omx.2019.100018.

[47] M.D. Chambers and D.R. Clarke. "Doped Oxides for High-Temperature Luminescence and Lifetime Thermometry". *Annual Review of Materials Research* 39.1 (2009), pp. 325–359. DOI: 10.1146/annurev-matsci-112408-125237. (Visited on 04/21/2021).

[48] Z. YinSheng et al. "Mn-ion-enhanced red spectral emission from yttrium aluminum garnet doped cerium phosphor". *Chinese Science Bulletin* 56 (2011). DOI: 10.1007/s11434-011-4780-9.

[49] V. Pankratov et al. "Luminescence of cerium doped YAG nanopowders". *Radiation Measurements* 42.4 (2007). Proceedings of the 6th European Conference on Luminescent Detectors and Transformers of Ionizing Radiation (LUMDETR 2006), pp. 679–682. DOI: 10.1016/j.radmeas.2007.02.046.

[50] C. Linderälv, D.l Åberg, and P. Erhart. "Luminescence Quenching via Deep Defect States: A Recombination Pathway via Oxygen Vacancies in Ce-Doped YAG". *Chemistry of Materials* 33.1 (2021). Publisher: American Chemical Society, pp. 73–80. DOI: 10.1021/acs.chemmater.0c02449.

[51] M. Borlaf et al. "Deep submicrometer YAG:Ce phosphor particles with high photoluminescent quantum yield prepared by flame spray synthesis". *Journal of the American Ceramic Society* 100.8 (2017), pp. 3784–3793. DOI: 10.1111/jace.14905.

[52] S. Hashmi et al. "4.10 - Thermal Spray Coating Processes". In: *Comprehensive Materials Processing*. Oxford: Elsevier, 2014, pp. 229–276. DOI: 10.1016/B978-0-08-096532-1.00407-6.

[53] H. Bloch and F. Geitner. "Chapter 8 - Repair and maintenance of rotating equipment components". In: *Machinery Component Maintenance and Repair (Fourth Edition)*. Fourth Edition. Gulf Professional Publishing, 2019, pp. 449–518. DOI: https://doi.org/10.1016/B978-0-12-818729-6.00008-3.

[54] P. Ctibor et al. "Plasma spraying of cerium-doped YAG". *Journal of Materials Research* 29.19 (2014), pp. 2344–2351. DOI: 10.1557/jmr.2014.251.

[55] Y. Kang et al. "Direct synthesis of strontium titanate phosphor particles with high luminescence by flame spray pyrolysis". *Materials Research Bulletin* 37.2 (2002), pp. 263–269. DOI: https://doi.org/10.1016/S0025-5408(01)00778-4.

[56] J. Kyeong Youl et al. "Size-dependent luminescent properties of hollow and dense BaMgAl10O17: Eu blue phosphor particles prepared by spray pyrolysis". *Korean Journal of Chemical Engineering* 21.5 (2004), pp. 1072–1080. DOI: 10.1007/BF02705595.

[57] I. Myronyuk et al. "Structural and Morphological Features of Disperse Alumina Synthesized Using Aluminum Nitrate Nonahydrate". *Nanoscale Research Letters* 11.1 (2016), p. 153. DOI: 10.1186/s11671-016-1366-0. (Visited on 05/12/2021).

[58] *Sigma Aldrich webpage - Retsch analytical sieve shaker*. https://www.retsch.com/products/sieving/sieve-shakers/as-200-control/function-features/. Accessed: 2021-06-14.

[59] M. Nasrollahzadeh et al. "Chapter 6 - Plant-Mediated Green Synthesis of Nanostructures: Mechanisms, Characterization, and Applications". In: *An Introduction to Green Nanotechnology*. Vol. 28. Interface Science and Technology. Elsevier, 2019, pp. 199–322. DOI: 10.1016/B978-0-12-813586-0.00006-7.

[60] K. Shankland. "An Overview of Powder X-ray Diffraction and Its Relevance to Pharmaceutical Crystal Structures". In: *Analytical Techniques in the Pharmaceutical Sciences*. New York: Springer New York, 2016, pp. 293–314. DOI: 10.1007/978-1-4939-4029-5_8.

[61] *Crystallography Open database*. http://www.crystallography.net/cod/search.html. Accessed: 2021-05-05.

[62] J. Goldstein et al. "Electron Beam—Specimen Interactions: Interaction Volume". In: *Scanning Electron Microscopy and X-Ray Microanalysis*. New York: Springer New York, 2018, pp. 1–14. DOI: 10.1007/978-1-4939-6676-9_1.

[63] J. Goldstein et al. "Backscattered Electrons". In: *Scanning Electron Microscopy and X-Ray Microanalysis*. New York: Springer New York, 2018, pp. 15–28. DOI: 10.1007/978-1-4939-6676-9_2.

[64] J. Goldstein et al. "Secondary Electrons". In: *Scanning Electron Microscopy and X-Ray Microanalysis*. New York: Springer New York, 2018, pp. 29–37. DOI: 10.1007/978-1-4939-6676-9_3.

[65] J. Goldstein et al. "SEM Image Interpretation". In: *Scanning Electron Microscopy and X-Ray Microanalysis*. New York: Springer New York, 2018, pp. 111–121. DOI: 10.1007/978-1-4939-6676-9_7.

[66] J. Goldstein et al. "X-Rays". In: *Scanning Electron Microscopy and X-Ray Microanalysis*. New York: Springer New York, 2018, pp. 39–63. DOI: 10.1007/978-1-4939-6676-9_4.

[67] C. Thomas. "Photoluminescence as function of Thickness". Unpublished paper, ESS confluence page. 2021.

[68] P. Smet, J. Van Haecke, and D. Poelman. "Spatially resolved cathodoluminescence of luminescent materials using an EDX detector". *Journal of Microscopy* 231 (2008), pp. 1–8. DOI: 10.1111/j.1365-2818.2008.02007.x. (Visited on 05/20/2021).

[69] L. Zheng et al. "Effect of particle size, transparency and light intensity on the color of powder". *IOP Conference Series: Earth and Environmental Science* 545 (2020), p. 012027. DOI: 10.1088/1755-1315/545/1/012027.

[70] H. Abou Oualid. "Efficient and Eco-Friendly Mechanical Milling Preparation of Anatase/Rutile TiO2-Glucose Composite with Energy Gap Enhancement". *Proceedings* 3 (2019). DOI: 10.3390/IOCN_2018-1-05497.

[71] G. Fagerlund. "Determination of specific surface by the BET method". *Materials and Structures* 6.33 (1973), pp. 239–245. DOI: 10.1007/BF02479039.